Reaction dynamics and hot nuclei formation in the $^{36}Ar+^{98}Mo$ reaction at 37*A* MeV studied through light charged particle and γ-ray emission

D. Santonocito,[1] P. Piattelli,[1] Y. Blumenfeld,[2] T. Suomijärvi,[2] C. Agodi,[1] N. Alamanos,[3] R. Alba,[1] F. Auger,[3] G. Bellia,[1,*] Ph. Chomaz,[4] M. Colonna,[1] R. Coniglione,[1] A. Del Zoppo,[1] P. Finocchiaro,[1] N. Frascaria,[2] A. Gillibert,[3] J. H. Le Faou,[2] K. Loukachine,[1,†] C. Maiolino,[1] E. Migneco,[1,*] J. C. Roynette,[2] P. Sapienza,[1] and J. A. Scarpaci[2]

[1]*INFN-Laboratorio Nazionale del Sud, Via S. Sofia 44, I-95123, Catania, Italy*

[2]*Institut de Physique Nucléaire,* IN_2P_3*-CNRS, F-91406 Orsay, France*

[3]*SPhN, DAPNIA, CEN Saclay, F-91191 Gif sur Yvette, France*

[4]*GANIL, BP 5027, F-14021 Caen, France*

(Received 2 August 2002; published 31 October 2002)

Central and mid-central collisions which lead to the formation of a heavy residue in the 37*A* MeV $^{36}Ar+^{98}Mo$ reaction have been studied with the MEDEA multidetector array coupled to a Parallel Plate Avalanche Counter. The dependence of the high energy gamma ray and light charged particle production as a function of the linear momentum transferred to the fused system has been studied. The unique potentialities of the MEDEA detector have made it possible to follow the evolution of the reaction dynamics from the pre-equilibrium stage to the formation of a heavy compound nucleus. The analysis of the correlation between the most energetic photons and protons shows how both of them are mainly produced in the most energetic primary nucleon-nucleon collisions. The multiplicity of high energy ($E_\gamma > 30$ MeV) γ rays has been found to increase with the linear momentum transfer, showing the dominance of two-body dissipation in the transfer mechanism and giving a tool to correlate the momentum transfer with the centrality of the collision. Light charged particle kinetic energy spectra show how in these collisions, compound systems with excitation energies of more than 3*A* MeV and temperature up to 7 MeV are formed. The experimental findings are compared with Boltzmann-Nordheim-Vlasov calculations. A scenario is found where the nucleus-nucleus interaction starts with two-body nucleon-nucleon collisions in the overlap region of nuclear densities. These collisions give rise to the production of high energy nucleons and γ rays, and play a fundamental role in the energy transfer from the relative motion to internal excitation of the quasiprojectile and the target.

DOI: 10.1103/PhysRevC.66.044619 PACS number(s): 25.70.−z

I. INTRODUCTION

The study of nuclei in extreme conditions is the most fascinating aspect of modern nuclear physics. This research is developed along three axes; spin, isospin, and temperature or excitation energy. Nucleus-nucleus collisions are a unique tool to produce nuclei at high temperature, reaching their limit of existence. It is of paramount importance to characterize as precisely as possible the hot nuclei produced in order to perform a detailed study of their behavior. This is a demanding task since dynamical effects play an important role in the formation of the excited nuclei role which increases with increasing bombarding energy.

Nucleus-nucleus collisions at low incident energy, below approximately 10*A* MeV, are mainly governed by statistical dissipative processes, fusion [1,2] and deep-inelastic reactions [3] being the dominant reaction mechanisms. At these energies the Pauli principle inhibits nucleon-nucleon collisions and the reaction dynamics are dominated by mean field effects. Most of the observed light particles and γ rays can be accounted for through the statistical decay of the reaction partners or the fused system. Conversely, in the relativistic energy regime, nucleon-nucleon collisions play a dominant role and the participant-spectator picture is applied to describe the reaction mechanism. In between, for bombarding energies $10A < E_{\rm beam} < 100A$ MeV, as soon as the relative momentum of the colliding nuclei approaches the value of the intrinsic Fermi momentum of the nucleons, the Pauli principle become less effective and the influence of the dinuclear mean field on the reaction dynamics is significantly modified by the effect of individual nucleon-nucleon collisions [4,5].

In this energy domain, complete fusion is no longer the dominant mechanism and reactions where only part of the kinetic energy of the projectile is transferred to the compound system take place [6–8]. Such reactions are essentially two body in nature, as a fast moving projectile remnant and a slower heavy excited recoil contain the bulk of the mass in the exit channel. In this paper we will call such reactions *incomplete fusion* reactions, since fusionlike residues exhibiting a large range of masses and linear momentum are produced [9–11] and the onset of preequilibrium particle and γ emission ascribed to nucleon-nucleon collisions is observed [12,13]. However, it must be kept in mind that substantial excitation energy may also be imparted to the projectile like nucleus, exhibiting some resemblance with the deep inelastic collisions well known at low bombarding energies [14,15]. The two massive excited entities, which subsequently decay according to statistical laws, are accompanied by a copious production of preequilibrium light

*Also at Dipartimento di Fisica dell'Universitá di Catania, Italy.

†Present address: Thomas Jefferson National Accelerator Facility, Newport News, VA.

particles and γ rays. It is therefore a difficult task to extract precisely the characteristics of the hot nuclei produced, such as spin, excitation energy, and temperature. The goal of this work is to obtain information on the first stage of the collisions and on the evolution toward a thermalized but highly excited system, through the detailed measurement of light charged particles and high energy γ rays emitted in coincidence with heavy fusionlike residues.

In recent years much experimental and theoretical effort has been devoted to the study of specific probes sensitive to the pre-equilibrium phase of the collisions. Extensive studies on the production of high energy γ rays ($E_\gamma > 30$ MeV) in heavy ion collisions at intermediate energies have shown how these photons originate from the most energetic first chance pn collisions that take place in the early stage of the nucleus-nucleus collision [16,17]. Such a hypothesis is supported by a wealth of inclusive data [16], that span a wide range of energy and mass of the system, and some exclusive data [18–22] that convincingly demonstrated the validity of the incoherent bremsstrahlung model. Since the photons, after their production, do not interact with the surrounding medium, they carry an unperturbed signal of the first stages of the nucleus-nucleus collision.

In this paper we will focus on central and midcentral collisions between heavy ions, at energies close to the Fermi energy (≈ 35 MeV), which lead to the formation of a heavy fusion residue. The unique characteristics of the MEDEA detector [23], which was designed to detect high energy γ rays and light charged particles simultaneously, will allow us to follow the evolution of the central collisions from the first stages of the nucleus-nucleus reaction, dominated by the emission of very energetic nucleons and photons, to the formation of an equilibrated hot system that eventually decays through the emission of low energy photons and thermalized particles.

In Sec. II the experimental setup and the data analysis procedures will be described. A detailed analysis of the light charged particle spectra will be presented in Sec. III, while in Sec. IV the analysis of the high energy gamma ray spectra will be presented and discussed. Section V will be devoted to the discussion of high energy protons and photons. The results of dynamical model calculations will be presented in Sec. VI and will be compared to experimental data. Finally conclusions will be drawn in Sec. VII.

II. EXPERIMENTAL METHODS

A. Experimental setup

The experiment was carried out at the Grand Accélérateur National d'Ions Lourds (GANIL) using an ^{36}Ar beam of 37*A* MeV with an average intensity of 1.5 pnA impinging on a 500 μg/cm^2 thick ^{98}Mo target. Light charged particles and gamma rays were measured in coincidence with fusionlike residues using the MEDEA multidetector [23] coupled to a square (14×14 cm^2) Parallel Plate Avalanche Counter (PPAC). A schematic view of the experimental setup is shown in Fig. 1.

The MEDEA multidetector, which was described in detail in Ref. [23], consists of a ball of 180 barium fluoride (BaF_2) scintillators and a forward wall of 120 plastic phoswich detectors. The 20 cm thick scintillators that compose the ball are placed at 22 cm from the target and cover the polar angles from 30° to 170°. They are arranged in eight rings of 24 detectors, each ring placed at a fixed polar angle and covering the whole azimuthal angle. The scintillators are wrapped with a 100 μm white teflon layer, to optimize the light collection, and a 50 μm mylar foil. The presence of this material in front of the detector introduces thresholds of 4 and 16 MeV on the detected protons and alpha particles, respectively. All the detectors cover the same solid angle of 63 msr with the exception of those of the forward ring which cover 32 msr. The forward plastic wall, which covers the polar angles between 10° and 30°, has a similar geometry with tapered detectors centered on the target. The phoswhich detectors are composed of a 2 mm thick ΔE fast scintillator (NE102A) backed by a 30 cm thick slow scintillator (NE115) that acts as an E detector and can stop protons up to 200 MeV. Plastic scintillators are arranged in five rings of 24 detectors each placed at a distance of 55 cm from the target. For these detectors a higher threshold, namely, 14 MeV for protons and 56 MeV for alphas, is introduced on the detected particles by the 2 mm thick ΔE detector. However particles stopped in ΔE, even if they cannot be identified, can still be taken into account in the light charged particle multiplicity spectra. The essential geometrical characteristics of each ring of detectors are summarized in Table I.

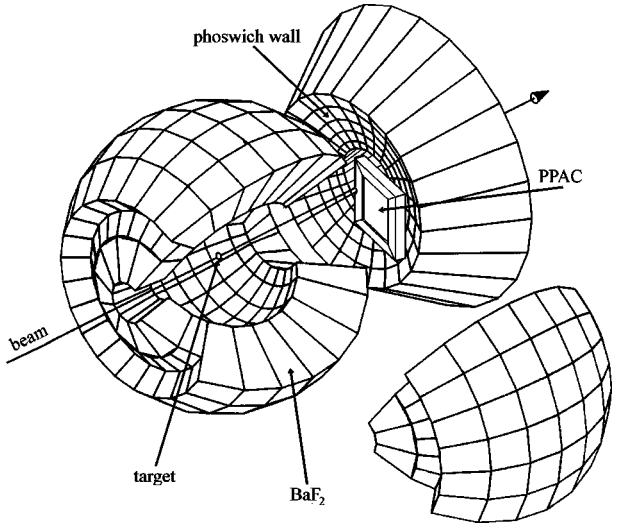

FIG. 1. Artist view of the experimental setup showing the MEDEA array and the forward PPAC detector.

The total geometrical efficiency of the array is 3.8π. The whole detector operates under vacuum inside a large scattering chamber to reduce the light charged particle detection thresholds.

To allow for particle and γ-ray identification in the BaF_2 detectors a pulse shape analysis of the photomultiplier analog signal and time of flight information was used. The BaF_2 signal was split into three outputs with different relative weights and was charge integrated adopting two different gates, a fast gate 30 ns long and a total energy gate 700 ns long. The total energy gate was used for two of the three

TABLE I. Main geometrical characteristics of the various detector rings of MEDEA. The detectors are either plastic phoswich detectors (PPD) or barium fluoride (BaF_2) scintillators.

Ring	Detector type	θ_{min}	θ_{max}	$\langle\theta\rangle$	$\Delta\phi$	Ω (msr)
1	PPD	10.0°	12.5°	11.2°	15°	2.2
2	PPD	12.5°	16.0°	14.2°	15°	3.9
3	PPD	16.0°	20.0°	18.0°	15°	5.6
4	PPD	20.0°	25.0°	22.5°	15°	8.6
5	PPD	25.0°	30.5°	27.7°	15°	11.5
6	BaF_2	30.5°	42.4°	36.5°	15°	31.8
7	BaF_2	42.4°	60.5°	51.5°	15°	63.2
8	BaF_2	60.5°	75.7°	68.1°	15°	63.2
9	BaF_2	75.7°	90.0°	82.8°	15°	63.2
10	BaF_2	90.0°	104.3°	97.1°	15°	63.2
11	BaF_2	104.3°	119.5°	111.9°	15°	63.2
12	BaF_2	119.5°	137.6°	128.5°	15°	63.2
13	BaF_2	149.5°	170.0°	159.7°	30°	60.8

outputs, allowing two different dynamic ranges corresponding approximately to 30 and 170 MeV of γ-ray equivalent full scale energy. The time of flight information with respect to the cyclotron rf with a resolution of ~ 1 ns was also measured. An example of a time of flight spectrum measured at 97.1° which clearly shows the separation between γ-rays and light particles is shown in Fig. 2.

A similar integration in two gates was also applied to the analog signals of the phoswich detectors to obtain a charge identification by means of ΔE-E correlations. The detector gains were adjusted in order to allow for the identification of charges up to $Z=8$ while retaining the isotope identification of the $Z=1$ particles.

The PPAC was located at 48 cm from the target in front of the phoswich detector wall and covered polar angles from 6° to 22°; part of the phoswich wall was therefore shadowed by this detector, reducing its geometrical efficiency. This PPAC yielded information on the energy loss and the time of flight, measured with respect to the cyclotron rf, of the detected heavy residues.

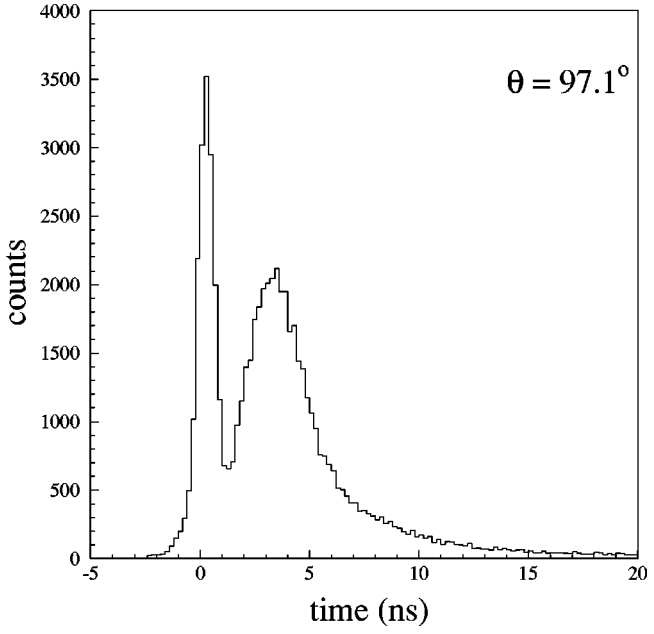

FIG. 2. Time of flight spectrum measured with a barium fluoride detector placed at 97.1°.

The trigger condition was given by the coincidence between the PPAC and at least one BaF_2 detector fired, with an energy threshold corresponding approximately to 2 MeV of γ-ray deposited energy. The coincidence trigger avoids contamination of the γ-ray energy spectra due to high energy cosmic ray events by requiring the occurrence of a reaction. However, a fraction of cosmic rays that is randomly in coincidence with true reaction events can still be present, but it was shown in the off-line analysis to be negligible.

A minimum bias run was also carried out during the measurement for normalization purposes. In this case the trigger condition was given by at least one BaF_2 or one phoswich detector firing with a low energy threshold. Using such a trigger condition, the measured reaction cross section amounts to 95% of the total reaction cross section.

B. Data reduction

The gamma energy calibration of BaF_2 was performed using the 4.4 and 6.1 γ-ray peaks from AmBe and PuC γ-ray sources and checked using as high energy reference point the 130-MeV γ-equivalent signal given by cosmic muons traversing the full detector length, obtained as described in Ref. [23]. The light charged particle calibration was deduced from the γ-ray one by adopting the prescriptions described in Ref. [24]. The particle energy was also corrected for the energy loss in the detector wrapping material. The full scale energy range was approximately 170 MeV for protons and 200 MeV for alpha particles.

Particle and γ-ray identification with the BaF_2 detectors was achieved in the off-line analysis by exploiting the ''Fast''–''Energy'' correlations and the time of flight information. An example of ''Time vs Energy'' and ''Fast vs Energy'' scatter plots for a detector placed at 82.8° are shown in Figs. 3(a)–3(b). By applying contours to both these planes an unambiguous identification of γ rays, protons, and alpha particles was achieved while deuterons were not separated from tritons.

In Fig. 3(a) the contours applied to select γ-rays and protons on the ''Time vs Energy'' scatter plot are shown. The ''Fast vs Energy'' scatter plots obtained retaining only those events inside the two contours are shown in Fig. 3(c) (γ rays) and Fig. 3(d) (protons). One observes that the time gate itself already selects all γ rays with a small contamination of high energy protons. Applying an additional contour, as shown in Figs. 3(c) and 3(d), yields a totally unambiguous γ-ray and proton identification. The same procedure was applied for the high gain energy range. Low energy charged particles, for which the fast component is too low and merges in the charge-to-digital converter pedestal, could not be isotopically identified. Consequently thresholds of 8 and 20 MeV were introduced off-line in the sorting of proton and α-particle spectra, respectively. However these low energy

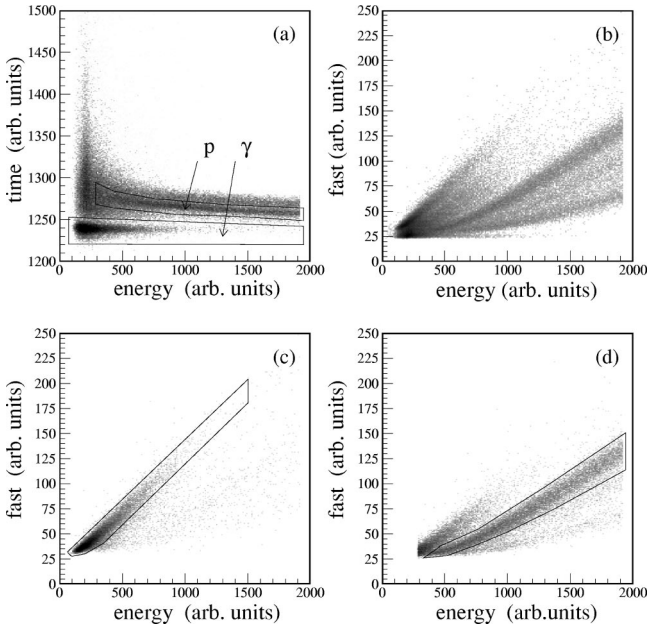

FIG. 3. Example of bidimensional correlation scatter plots, that allow for particle identification with the BaF_2 detector. The data are relative to a detector placed at 82.8°. (a) ''Time'' vs ''total energy'' scatter plot shows the good time resolution allowing a clear separation between γ rays and light charged particles. The two contours shown are the selection cuts for γ rays and protons. (b) ''Fast'' vs ''total energy'' scatter plot for the same BaF_2 detector showing the separation among protons, deuterons and tritons together and alpha particles. (c) ''Fast'' vs ''total energy'' scatter plot sorted selecting the γ-ray events with the cut of panel (a). (d) ''Fast'' vs ''total energy'' scatter plot sorted selecting the proton events with the cut of panel (a).

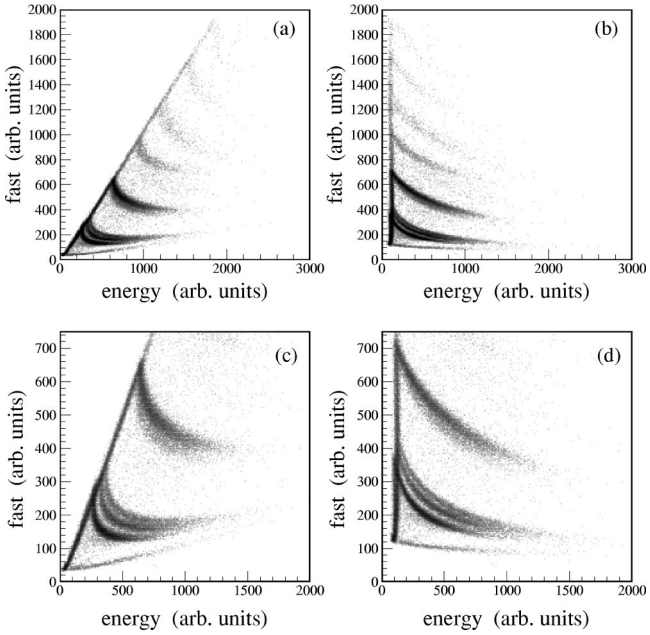

FIG. 4. a) ''Fast'' vs ''total energy'' scatter plot for a phoswich detector showing charged particles separation up $Z=7$. (c) A zoom on the low ''fast'' region of the same detector shows the mass resolution for $Z=1$ particles. (b) and (d) are the same as (a) and (c), respectively, after the correction for the signal mixing that gives the true ΔE-E response (see the text for details).

particles were still taken into account in the light charged particle multiplicity.

For the phoswich detectors particle identification was achieved by applying cuts on the ΔE-E (Fast-Energy) plane. In the fast-energy representation [Fig. 4(a)] the data occupy a region of the plane in between two lines that cross at an angle smaller than 90°. This is due to the mixing of the fast and slow components in the two integration gates. The two lines correspond to events in which the particles have been stopped in the ΔE detector and events without the ΔE signal (neutral particles), respectively. To remove this mixing we have adopted the method described in Ref. [25] which allows the extraction of the true ΔE and E signals [Fig. 4(b)]. Light charged particles were identified up to $Z=7-8$ in most of the phoswich detectors [Figs. 4(a) and 4(b)], and isotopes were clearly separated for $Z=1$ [Figs. 4(c) and 4(d)]. The energy calibration was deduced from a calibration run performed using monoenergetic particles taking as reference values the punch through energies of protons and α particles.

C. Event selection

A scatterplot of energy loss vs time of flight measured in the PPAC for heavy residues is shown in Fig. 5. The broad distribution that can be seen at large energy losses can be associated with fusionlike events similarly to what has been previously observed in the $^{36}Ar+^{90}Zr$ reaction at 27A MeV studied with the same detector setup [26], and in similar reactions with an analogous recoil detection system [27,28]. Here a higher threshold was set on the energy loss signal to eliminate events associated with peripheral reactions. Only

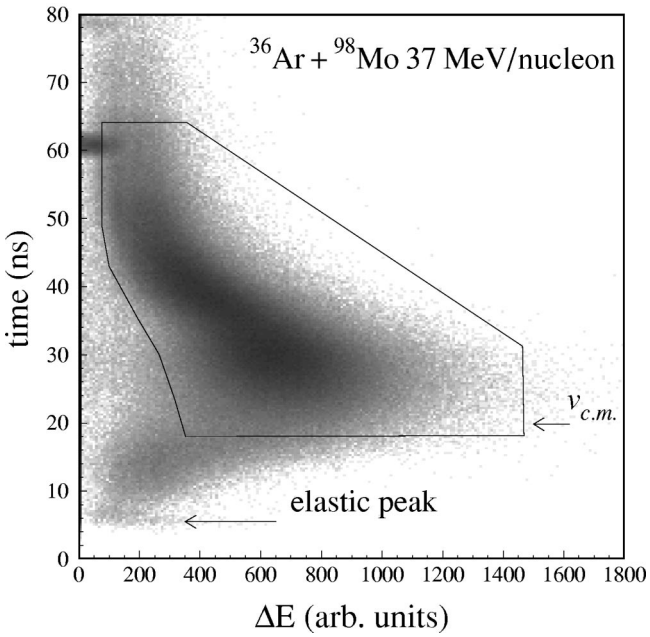

FIG. 5. Two dimensional ''energy loss'' vs ''time of flight'' scatter plot obtained from the PPAC. The fusion-like residue events that were retained for the analysis are enclosed in the contour line.

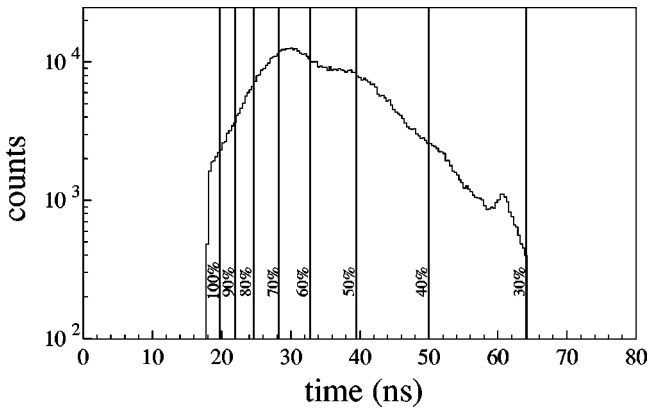

FIG. 6. Velocity spectrum of the evaporation residues detected in the PPAC. Vertical lines correspond to the different velocity bins adopted in the analysis.

the fusion-like events enclosed in the contour shown in the figure were retained in the analysis. The time of flight spectrum was calibrated using a time calibrator and the elastic peak position was obtained in a run with the PPAC in trigger and the ''op'' of all MEDEA detectors in anticoincidence.

The time spectrum observed (Fig. 6) shows a broad distribution of residue velocities with a mean value corresponding to 58% of the center of mass velocity, which corresponds to 50% of linear momentum transferred to the residue, a value lower than predicted by the Viola systematics [7] for incomplete linear momentum transfer. These systematics rely on measurements with light projectiles ($A \leqslant 20$); in particular above 20*A* MeV the results were taken from measurements using α particles. Departures from these systematics were already observed in previous experiments where a dependence of the momentum transfer on projectile mass and on system asymmetry was found using ^{40}Ar as a projectile [29].

The width of the time spectrum reflects the fact that many different linear momentum transfers are populated in the reaction at a single bombarding energy, which is one of the attractive features of intermediate energy heavy ion collisions. By gating on the recoil velocity, one will be able to study reactions with different linear momentum transfers and different deposited excitation energies. However, it must be kept in mind that the distribution is also broadened by particle evaporation, the more so at the highest velocities which are expected to correspond to the highest excitation energies for which evaporated particle multiplicities will be the largest. Nevertheless, previous experiments performed by detecting light charged particles in coincidence with a heavy residue at similar bombarding energies [13,27,28,30] have shown that the event selection in terms of residue velocity is able to select collisions characterized by a different centrality; in normal kinematics central collisions give rise to a larger linear momentum transfer and therefore to higher velocities of the residue, the maximum being reached in complete fusion events.

In the present study, the emission of γ rays and light charged particles is investigated as a function of the detected recoil velocity. The velocity spectrum of the evaporation residues was analyzed in terms of the ratio of the residue velocity to center of mass velocity $v_R/v_{\mathrm{c.m.}}$. It was divided into seven bins (Fig. 6) whose average velocities are reported in Table II. A first indication of the evolution of the dynamics as a function of the recoil velocity can be deduced from the trend of light charged particle multiplicities detected in MEDEA. As shown in Fig. 7 the raw light particle multiplicity increases as a function of the recoil velocity. Since light particle multiplicity is known to be a good indicator of the centrality of the collision it already appear that gating on large recoil velocity selects events of increasing centrality.

TABLE II. Bin limits and average velocity values (columns 2 and 3) for the seven velocity bins used in the data sorting.

Velocity bin	$v_R/v_{\mathrm{c.m.}}$ limits	$\langle v_R/v_{\mathrm{c.m.}} \rangle$
V37	0.30–0.40	0.37
V45	0.40–0.50	0.45
V55	0.50–0.60	0.55
V65	0.60–0.70	0.65
V73	0.70–0.80	0.73
V85	0.80–0.90	0.85
V93	0.90–1.00	0.93

III. ANALYSIS OF THE LIGHT CHARGED PARTICLE SPECTRA

At intermediate bombarding energies light charged particles are emitted throughout the whole nucleus-nucleus collision with different time scales: from the first phase, when the emission of the most energetic particles takes place, to a later stage when thermal equilibrium is reached and statistically emitted particles cool down the excited fragments. A deeper knowledge of the collision dynamics and the evolution from a preequilibrium stage toward a thermalized system can be obtained from the investigation of the light

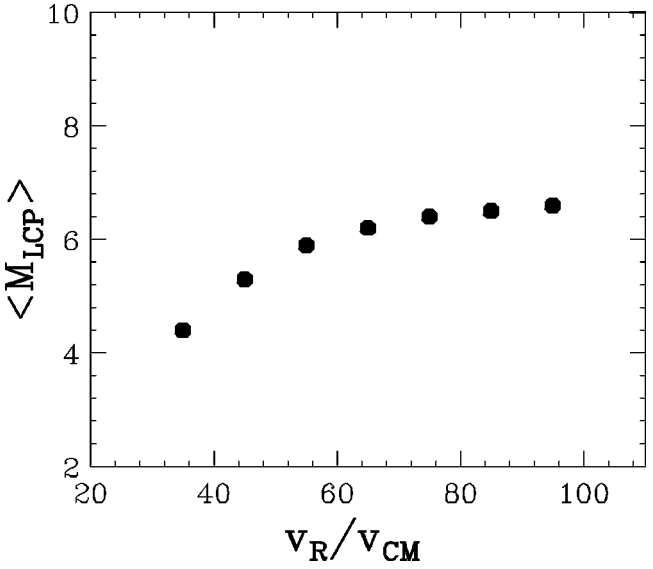

FIG. 7. Evolution of the raw light charged particle multiplicity as a function of the recoil velocity.

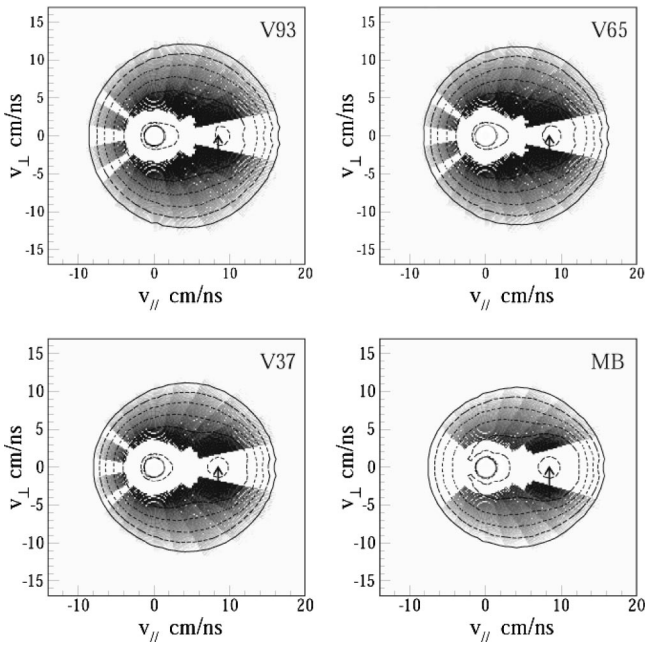

FIG. 8. Galilei-invariant proton cross section as a function of the velocity components parallel and perpendicular to the beam direction. The distributions shown refer to the V37, V65, and V93 bins and to the minimum bias (MB) run.

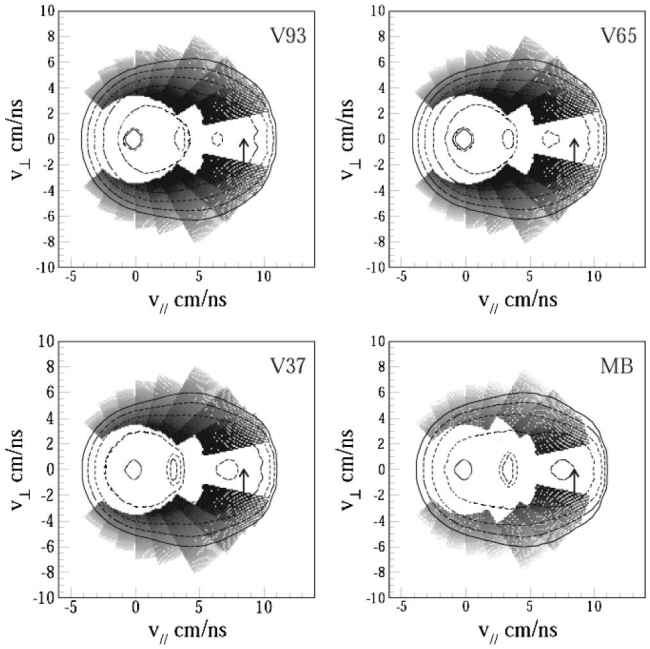

FIG. 9. Galilei-invariant alpha cross section as a function of the velocity components parallel and perpendicular to the beam direction. The distributions shown refer to the V37, V65, and V93 bins and to the minimum bias (MB) run.

par5ticle energy spectra, provided that one is able to disentangle the different sources. Therefore, light charged particle energy spectra emitted in coincidence with the evaporation residues were sorted according to the velocity bins previously mentioned and analyzed in terms of different emitting sources.

A. Identification of the light charged particle sources

As a first step, in order to identify the sources contributing to the particle emission, two-dimensional Galilei-invariant velocity distributions were plotted as a function of the velocity components parallel and perpendicular to the beam direction ($v_\parallel$, $v_\perp$) for protons, and alpha particles. This representation allows us to clearly localize in terms of $v_\parallel$ the position of the different sources since they manifest themselves as circles centered at different $v_\parallel$ values. If the events selected encompass a range of source velocities, the loci of the particles will be diffuse ellipses rather than circles. As an example, Figs. 8 and 9 show the two-dimensional Galilei-invariant velocity distributions for protons and alpha particles detected in coincidence with residues belonging to the velocity bins characterized by $v_R/v_{\mathrm{c.m.}}$ 0.93, 0.65, and 0.37 together with the results from the minimum bias data set. Two sources can be clearly identified: a slow source and a fast source with a velocity close to the projectile velocity (8.75 cm/ns indicated by an arrow in the figure). The relative intensities of these two sources change as a function of the recoil velocity; in particular from the highest to the lowest velocity bin an increase of the contribution from the fast source can be seen. This contribution is even larger for the minimum bias data set. However, these two sources are not sufficient to explain all the observed yield and the introduction of a third mid-velocity source is therefore necessary. This source can be identified in the proton velocity distributions as giving rise to the highest transverse velocity par-

TABLE III. Multiplicities, temperatures, and velocities of the fast source extracted from the moving source fits for protons and alpha particles. MB stands for minimum bias data set.

Bin	$\langle v_R/v_{\mathrm{c.m.}}\rangle$	M_p	T_p (MeV)	$(v/c)_p$	M_α	T_α (MeV)	$(v/c)_\alpha$
V37	0.37	0.78±0.04	3.9±0.1	0.28±0.01	1.20±0.06	5.4±0.1	0.24±0.01
V45	0.45	0.72±0.04	4.1±0.1	0.28±0.01	1.10±0.05	5.5±0.1	0.24±0.01
V55	0.55	0.73±0.04	4.2±0.1	0.28±0.01	1.00±0.05	5.7±0.1	0.23±0.01
V65	0.65	0.70±0.03	4.2±0.1	0.28±0.01	0.90±0.05	5.8±0.1	0.23±0.01
V73	0.73	0.69±0.03	4.2±0.1	0.28±0.01	0.80±0.04	5.8±0.1	0.24±0.02
V85	0.85	0.68±0.03	4.3±0.1	0.28±0.01	0.70±0.04	6.0±0.1	0.23±0.02
V93	0.93	0.67±0.04	4.3±0.1	0.28±0.01	0.60±0.04	6.1±0.1	0.23±0.02
MB	–	0.70±0.03	3.6±0.1	0.28±0.01	0.54±0.04	5.0±0.1	0.25±0.02

TABLE IV. Multiplicities, temperatures, and velocities of the intermediate velocity source extracted from the moving source fits for protons and alpha particles.

Bin	$\langle v_R/v_{\text{c.m.}}\rangle$	M_p	T_p (MeV)	$(v/c)_p$	M_α	T_α (MeV)	$(v/c)_\alpha$
V37	0.37	1.22±0.05	10.4±0.1	0.14±0.01	1.00±0.05	11.6±0.1	0.14±0.01
V45	0.45	1.60±0.08	10.6±0.1	0.14±0.01	1.10±0.06	11.6±0.1	0.15±0.01
V55	0.55	1.74±0.09	11.1±0.1	0.14±0.01	1.10±0.06	11.6±0.2	0.15±0.02
V65	0.65	1.94±0.09	11.4±0.1	0.14±0.02	1.20±0.07	11.7±0.2	0.15±0.02
V73	0.73	2.00±0.10	11.7±0.2	0.14±0.02	1.20±0.06	11.5±0.1	0.15±0.02
V85	0.85	2.00±0.10	12.0±0.2	0.13±0.02	1.20±0.07	11.4±0.1	0.15±0.02
V93	0.93	1.92±0.09	12.2±0.2	0.13±0.02	1.30±0.07	11.6±0.2	0.15±0.02
MB	-	0.50±0.03	10.1±0.1	0.14±0.01	0.63±0.03	11.3±0.1	0.15±0.01

ticles. In the alpha velocity distribution this source is less evident but it will be shown that its presence is needed in order to obtain a reasonable fit to the energy spectra.

B. Analysis in term of moving source fit

In order to extract information about velocities, emitted particle multiplicities and temperatures of the different sources and gain a deeper understanding of the evolution of the system towards thermal equilibrium, the experimental light charged particle kinetic energy spectra were reproduced by a moving source fit in which the particles are assumed to be emitted isotropically from three moving sources. The energy distribution of the emitted particles were parametrized, in the source rest frame, adopting a surface-type Maxwellian distribution given by

$$\frac{d^2M}{d\Omega dE} = \frac{M}{4\pi T^2}(E-E_c)\exp[-(E-E_c)/T], \qquad (1)$$

where E_c is the Coulomb barrier of the particle, T is the source temperature and M is the multiplicity. The Maxwellian distribution is then transformed in the laboratory reference frame in order to carry out the fit of the spectra using the relation

$$\left[\frac{d^2M}{d\Omega dE}\right]_{lab} = \left(\frac{E_{lab}}{E'}\right)^{1/2}\left[\frac{d^2M}{d\Omega dE}\right]_{E=E'}, \qquad (2)$$

where the particle energy E' in the source reference frame is given by

$$E' = E_{\text{lab}} + E_s - 2(E_{\text{lab}}E_s)^{1/2}\cos\theta_s, \qquad (3)$$

where E_s indicates the energy of a particle moving with the source velocity.

The spectra were analyzed assuming three sources parametrized as Eq. (1): fast, slow, and intermediate velocity sources. The fitting was performed using a χ^2 minimization procedure. In the fitting procedure the multiplicities, temperatures and velocities of all the sources have been left as free parameters, while the values of the Coulomb barriers were fixed to 1, 1, and 4 MeV for the fast, intermediate, and slow velocity sources, respectively, in the case of protons and to 2, 4 and 10 MeV in the case of alpha particles. Note that the sensitivity of the fit to small changes of the Coulomb barrier values for the intermediate and the fast source is small.

The particle spectra were simultaneously fit with the superposition of the three sources. In the case of alpha particles the energy spectra at angles larger than 90° can be reasonably reproduced using only the slow source. For this reason, the fit procedure was performed in two successive steps: first of all a fit procedure using a single surface-type Maxwellian source was performed to analyze the alpha particle spectra beyond 90°, then the deduced values of temperature and velocity were adopted as fixed parameters in the three moving source fits. The extracted parameters (multiplicity, temperature and source velocity) for the fast, intermediate and

TABLE V. Multiplicities, temperatures, and velocities of the slow source extracted from the moving source fits for protons and alpha particles.

Bin	$\langle v_R/v_{\text{c.m.}}\rangle$	M_p	T_p (MeV)	$(v/c)_p$	M_α	T_α (MeV)	$(v/c)_\alpha$
V37	0.37	1.49±0.07	5.1±0.2	0.028±0.004	0.80±0.04	5.7±0.2	0.030±0.003
V45	0.45	1.66±0.08	5.3±0.2	0.036±0.005	1.00±0.05	5.8±0.2	0.036±0.004
V55	0.55	1.82±0.08	5.4±0.2	0.040±0.005	1.30±0.06	6.0±0.2	0.040±0.004
V65	0.65	1.93±0.09	5.5±0.2	0.043±0.005	1.50±0.07	6.2±0.2	0.043±0.004
V73	0.73	1.99±0.09	5.8±0.2	0.047±0.005	1.60±0.07	6.5±0.2	0.046±0.005
V85	0.85	2.00±0.10	6.0±0.2	0.050±0.005	1.70±0.09	6.7±0.2	0.048±0.005
V93	0.93	2.06±0.10	6.2±0.2	0.052±0.005	1.80±0.09	6.9±0.2	0.050±0.005
MB	-	0.49±0.03	5.8±0.2	0.040±0.004	0.28±0.02	6.7±0.2	0.042±0.004

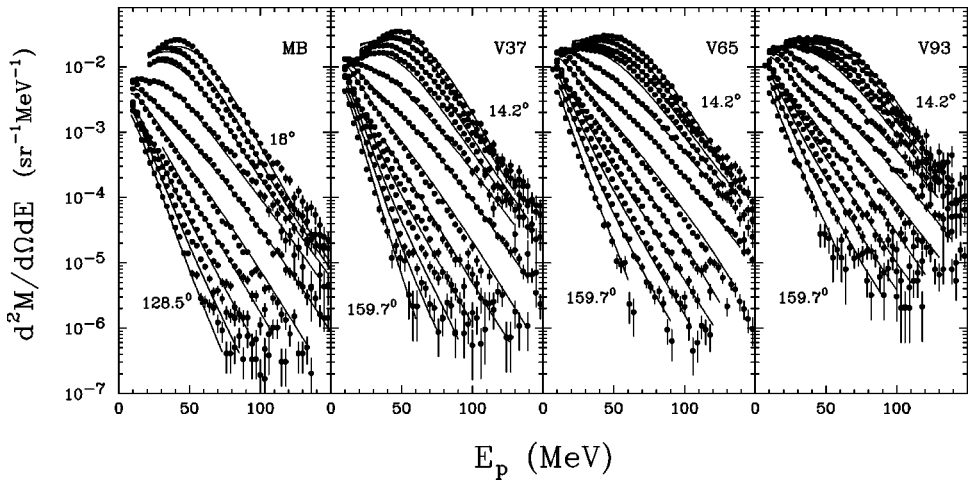

FIG. 10. Proton energy spectra measured at laboratory angles ranging from 14.2° to 159.7° in the minimum bias (MB) run and in coincidence with evaporation residues for different velocity bins. The solid lines are the result of the moving source fit described in the text.

slow velocity sources are listed in Tables III, IV, and V, respectively. The uncertainties quoted correspond to the change in a parameter that increases χ^2 by 1, with all the other parameters fixed at their optimum values [31]. Representative proton and alpha spectra and associated fits (solid lines) for different velocity bins are shown in Figs. 10 and 11; the agreement is excellent for all velocity bins in the whole angular range covered.

In order to point out the evolution of relative contributions of the different sources as a function of the detection angle the contributions relative to each of the three sources and their overall sum are presented for the V65 velocity bin (0.65 $v_{\mathrm{c.m.}}$) in Figs. 12 and 13. The fast source component (dot-dashed curve), which represents the dominant contribution to the total yield at forward angles, progressively decreases with increasing polar angle and becomes negligible beyond 60°. The slow source component (dashed curve) governs the low energy part of the spectra beyond 30° becoming increasingly important at backward angles. The intermediate velocity component (dotted) contributes strongly to the high energy part of the spectra; actually it is the only source giving a significant contribution to the proton spectra above 40 MeV for angles greater than 42.4°. Figures 14 and 15 show the evolution of the relative contributions of the three sources for protons and alphas as a function of different velocity bins at forward (22.5°) and backward (111.9°) angles. Proton spectra at forward angles (top panels in Fig. 14) show a marked increase of the intermediate velocity source contribution (dotted) as a function of $v_R/v_{\mathrm{c.m.}}$ while at backward angles (bottom panels Fig. 14) the relative contribution of the two sources (slow and intermediate) is rather constant. Alpha particle spectra at forward angles (top panels in Fig. 15) show a trend similar to that previously observed for proton spectra. At backward angles the spectra are dominated by the emission of the slow source with the intermediate source giving only a small contribution.

Deuterons and tritons also carry a significant fraction of the total momentum. Unfortunately, as indicated in Sec. II B, it was not possible experimentally to separate these two species in the BaF_2 detectors. Therefore, deuteron and triton spectra were only fitted at forward angles covered by the phoswich detectors ($\theta_{lab}<30°$), where the projectilelike contribution is dominant, to extract temperature, velocity and the multiplicities M_d and M_t of deuterons and tritons, respectively. For larger angles a fit of the sum spectra of deuterons plus tritons was performed assuming an effective particle mass equal to $(2\cdot M_d+3\cdot M_t)/(M_d+M_t)$. Source velocities were fixed to the values extracted from the proton and α-particle spectra analysis. This approximate procedure was adopted with the aim of estimating the deuteron and

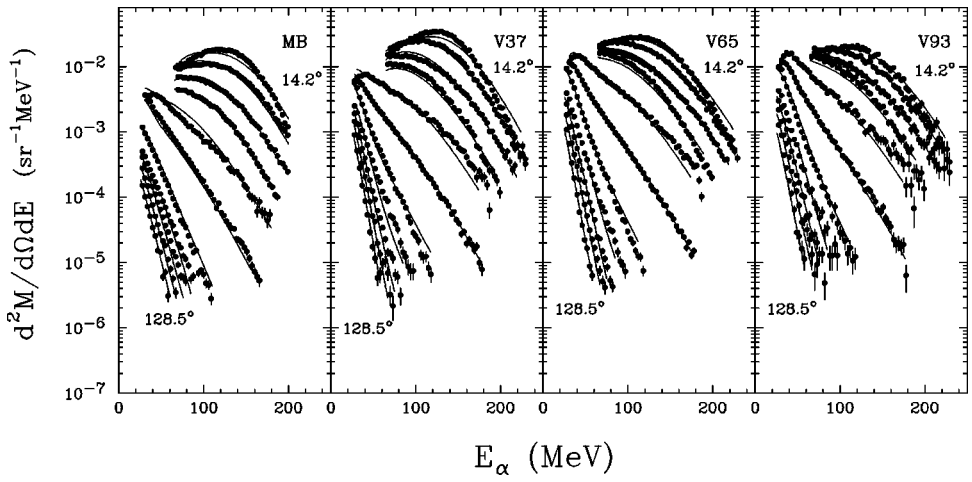

FIG. 11. Alpha particle energy spectra measured at laboratory angles ranging from 14.2° to 128.5° in the minimum bias (MB) run and in coincidence with evaporation residues for different velocity bins. The solid lines are the result of the moving source fit described in the text.

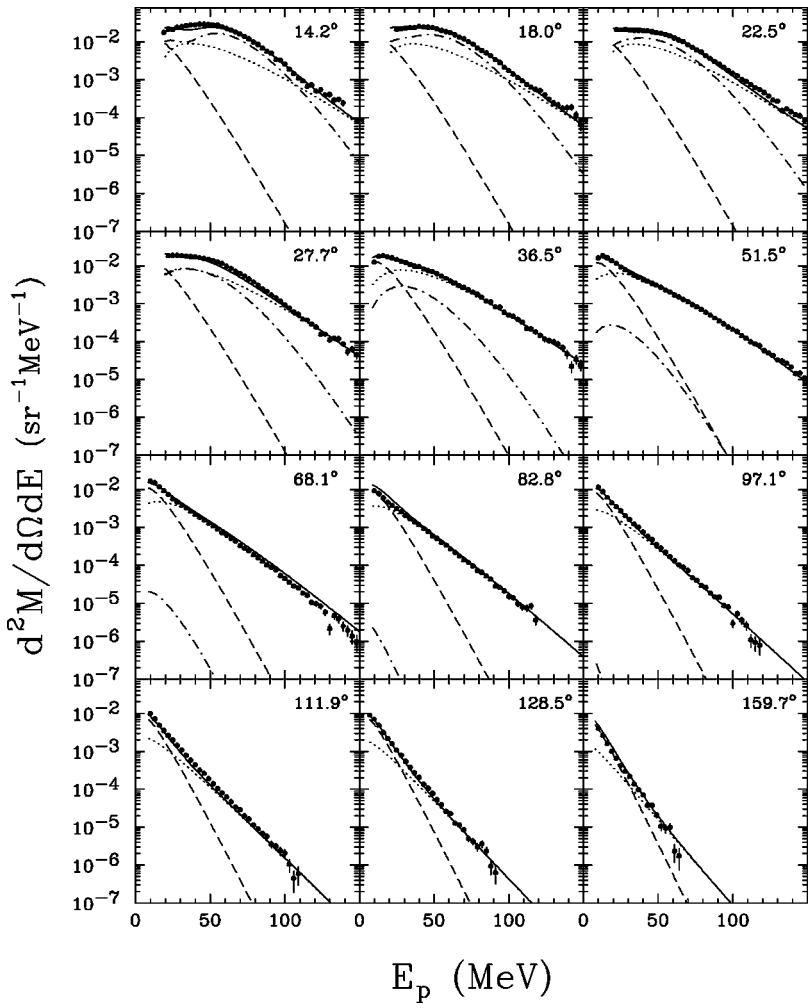

FIG. 12. Contributions of the three Maxwellian sources adopted in the fit to the proton spectra detected in coincidence with evaporation residues belonging to the V65 velocity bin for all the detection angles in the laboratory frame. The contribution of the evaporation residue is shown by the dashed curve, the intermediate velocity source by the dotted line, and the projectilelike source by the dot-dashed curve. The solid line is the result of their sum.

triton multiplicities and temperatures of the intermediate source to be used to evaluate the excitation energy and the mass of the hot recoiling nucleus formed in incomplete fusion events prior the evaporation stage which, from now on, we will call primary residue. However, its reliability was also checked by simulations. The results of the fit indicate that the multiplicity of nucleons associated to the emission of deuterons and tritons from the fast source ranges from 2.4 to 1.8 decreasing with increasing residue velocity. The contribution of the intermediate source ranges from 2 to 3.6 nucleons emitted, while the temperature is almost constant as a function of residue velocity ranging from 11 to 11.7 MeV.

C. Interpretation of the three sources

Moving source fits to particle energy spectra have been widely used in the determination of the temperatures of emitting sources [13,28,32,33]. The extent to which the sources used in the fits represent real physical sources for which a temperature can be defined, or are merely a good parametrization able to describe a mixture of processes is often not clear. In this case, the slow source can be ascribed with confidence to a real physical source which is the excited recoiling nucleus, the residue of which is detected in the PPAC. The fast source may either correspond to an excited projectilelike nucleus which decays in flight, or to an ensemble of nucleons and alpha particles which originate from the projectile and have only weakly interacted during the collision. The introduction of an intermediate velocity source is a convenient way to mimic the emission of pre-equilibrium particles, but can in no way be interpreted as a thermalized excited nucleus decaying by light particle emission. This point will be clarified in the following where we will describe in detail the behavior of the proton and α-particle sources as a function of the recoil velocity. To allow a quick comparison of the results of the fits, the values of multiplicity, temperature and velocity extracted from the fits are reported in Fig. 16.

1. Fast source

The fast source exhibits a rather constant velocity value as a function of $v_R/v_{\mathrm{c.m.}}$. In the proton, deuterons and tritons fits it is approximately equal to the beam velocity, while alpha particles fits give a slightly smaller velocity value, but still very close to beam velocity ($v_{beam}/c=0.28$).

Particle multiplicity values decrease as a function of the ratio $v_R/v_{\mathrm{c.m.}}$. This trend is more evident in the case of alpha particles than for all $Z=1$ particles, and is consistent with an interpretation of this source as a projectilelike source

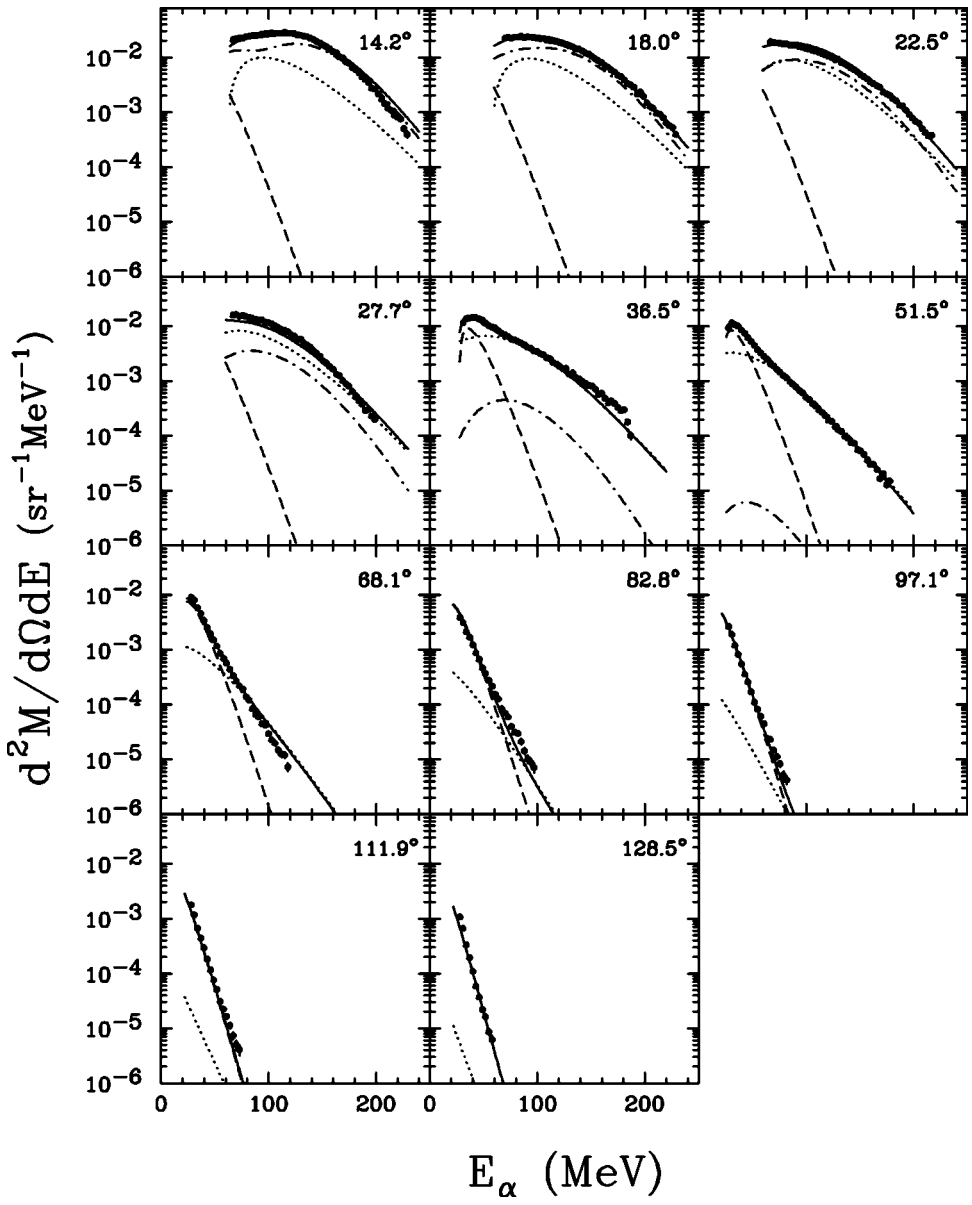

FIG. 13. Evolution of the relative contributions of the three Maxwellian sources adopted in the fit to the proton spectra at forward ($\theta = 22.5°$) and backward $\theta = 111.9°$ angles. The contribution of the evaporation residue is shown by the dashed curve, the intermediate velocity source by the dotted line, and the projectilelike source by the dot-dashed curve. The solid line is the result of their sum.

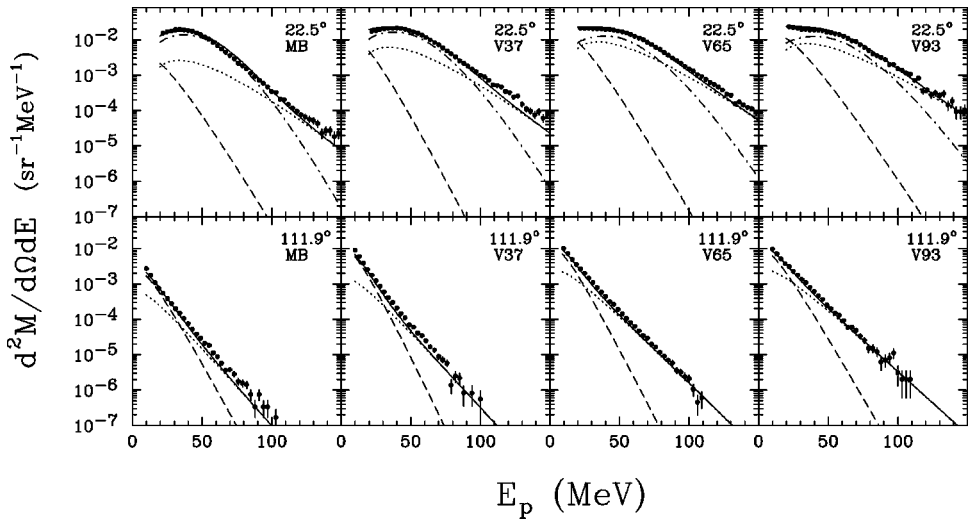

FIG. 14. Contributions of the three Maxwellian sources adopted in the fit to the alpha particle spectra detected in coincidence with evaporation residues belonging to the V65 velocity bin for all the detection angles in the laboratory frame. The contribution of the evaporation residue is shown by the dashed curve, the intermediate velocity source by the dotted line, and the projectilelike source by the dot-dashed curve. The solid line is the result of their sum.

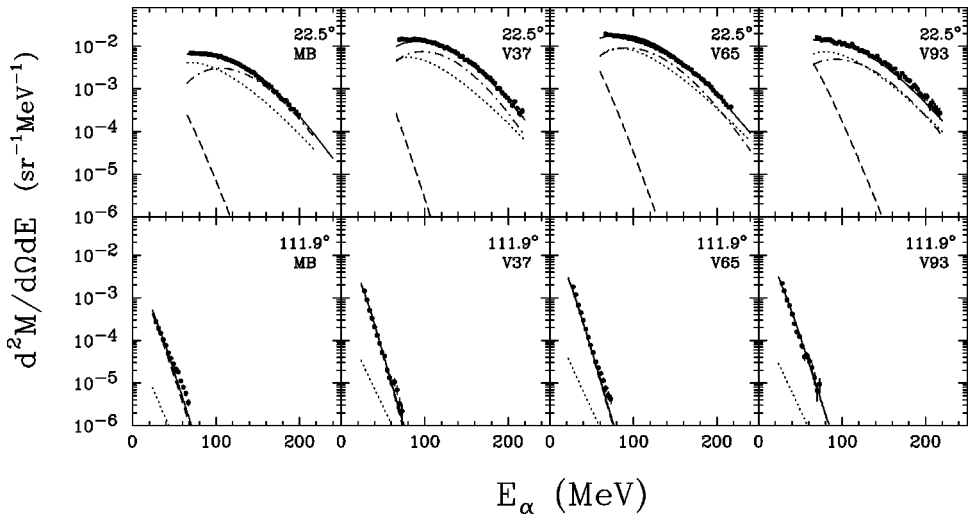

FIG. 15. Evolution of the relative contributions of the three Maxwellian sources adopted in the fit to the alpha spectra at forward ($\theta = 22.5°$) and backward $\theta = 111.9°$ angles. The contribution of the evaporation residue is shown by the dashed curve, the intermediate velocity source by the dotted line, and the projectilelike source by the dot-dashed curve. The solid line is the result of their sum.

whose contribution decreases with the increase of the centrality of the reaction: larger residue velocities are interpreted as due to larger massive transfer taking place in more central collisions which leave smaller projectilelike residues. In principle in this scenario one would expect the projectilelike contribution to vanish for the most central collisions. Surprisingly enough we still observe a non-negligible contribution of the fast source even for the fastest residue velocity bin, which, as we will show later in Sec. V, corresponds to collisions in which the complete overlap of the projectile with the target is reached. However, in Refs. [11,34] it was shown how an extended concept of the projectilelike source should be taken into account in the case of central collisions in the ^{40}Ar+$^{\text{nat}}$Ag reaction at 34*A* MeV, to include also ejectiles which retain some memory of the translational motion of the projectile, but are almost directly ejected from the collision zone. This idea of ''source'' is quite different from that of a heated projectilelike fragment emerging from the collision zone and undergoing an evaporation-like decay, the latter process being surely important for peripheral collisions.

The striking feature, however, is represented by the large alpha particle multiplicities compared to those for protons. Large cross sections for multialpha events have already been observed in peripheral collisions involving light and medium light projectiles, such in the case of the ^{35}Cl+^{197}Au reaction at 30*A* MeV [35]. A possible explanation for this observation can be a sudden breakup of an excited quasiprojectile formed in the reaction, in particular in the present case where the ^{36}Ar projectile may well exhibit an α particle substructure.

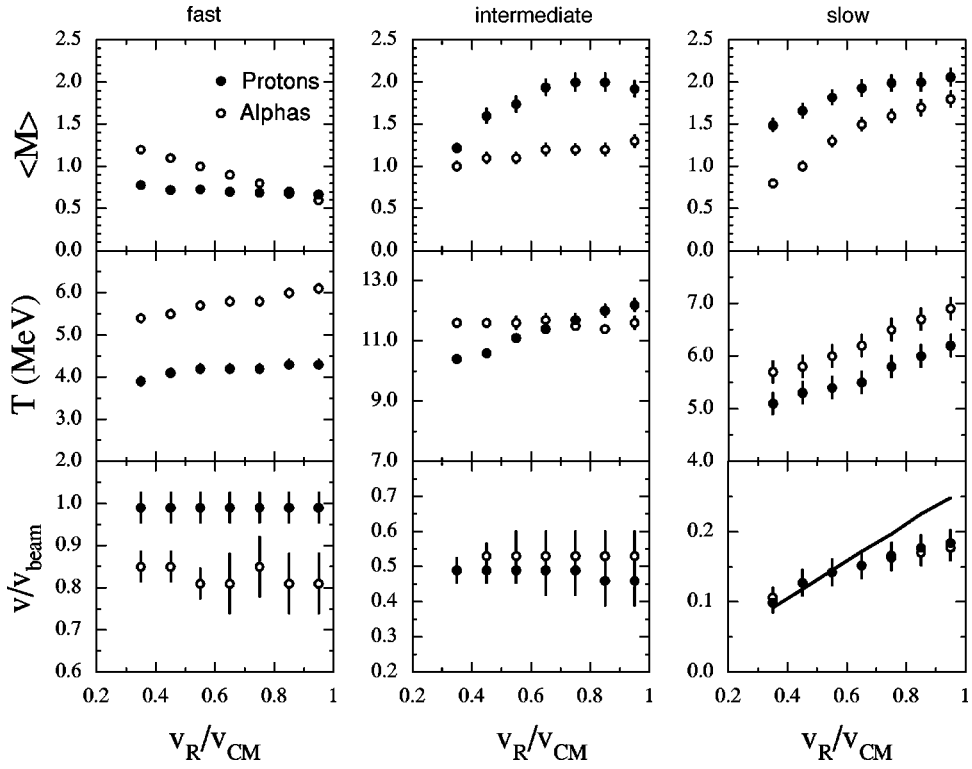

FIG. 16. Summary of the results obtained from protons and alphas fit for different velocity bins. Velocities, temperatures, and multiplicities of the fast, intermediate, and slow sources, respectively, are shown as a function of the $v_R/v_{\text{c.m.}}$ ratio. Full symbols refer to protons, while open symbols refer to alphas. The full line in lower panel shows the trend of the recoil velocity measured with the PPAC.

This mechanism can also explain the anomalously large temperatures observed for alpha particles which range from 5.4 to 6.1 MeV with a small dependence on the velocity of the heavy residue. Lower temperature values, with a weaker dependence on $v_R/v_{\mathrm{c.m.}}$ are instead observed for protons. These values are in good agreement with the observations made in similar reactions for the projectilelike source in case of proton [13] and neutron [36] spectra.

2. Slow source

The velocities of the slow source extracted from the fits of all light charged particle spectra are equal within the error bars. Moreover these values are in remarkable agreement with the measured recoil velocity up to $v_R/v_{\mathrm{c.m.}}=0.65$ (solid line in Fig. 16). This result gives confidence in the validity of the fit procedure, and supports the interpretation of this source as the compound nucleuslike source. The disagreement observed for larger values of $v_R/v_{\mathrm{c.m.}}$, where the fits tends to give values below the measured residue velocity, could be interpreted in terms of a saturation of the momentum transfer; in this scenario the fastest residues would not be correlated to an almost complete momentum transfer but to velocity fluctuations following a large amount of particle emission.

Proton and alpha particle multiplicities and temperatures increase as a function of the residue velocity. These results are in agreement with the interpretation of a heavy residue whose excitation energy and mass increase as a function of the recoil velocity and support the picture of an incomplete fusion reaction giving rise to more and more excited compound systems with increasing violence of the collision. The temperature and multiplicity values extracted from the fits of alpha particle spectra are very similar to those reported for the Ar+Ag reactions studied between 27 and 60 *A* MeV where a heavy residue was detected in coincidence with light charged particles [37]. The value of almost 7 MeV reported in Ref. [38] deduced from analysis of alpha spectra in the most central collisions, points to a saturation of the heavy residue temperature and therefore of the excitation energy. As a further evidence of this effect, similar results were also obtained using the reaction $^{84}\mathrm{Kr}+^{197}\mathrm{Au}$ at 32*A* MeV [38].

Temperature values for the compound nucleus like source extracted from particle spectra increase from a value of 5 MeV up to 6.2 MeV for protons and from 5.7 to 6.9 MeV for alpha particles. However the ratio T_α/T_p remains constant at a value of ~ 1.1 over the whole range explored. This can be understood if one considers that these measured ''apparent temperatures'' represent a weighted average over the entire deexcitation cascade. In the case of α particles, which are preferentially emitted in the first steps of the cascade, one expects the observed value to be closer to the initial temperature of the fusionlike nucleus. This interpretation is confirmed by the findings of Gonin *et al.* [39], who investigated the dependence of the apparent temperature on the particle species in the reaction Ni+Mo at 550 and 655 MeV bombarding energies. Although, based on these considerations, one may expect the initial temperatures to be slightly higher than those measured from α-particle spectra, we will adopt in the following the conservative approach of assumimg T_α as temperature of the fusionlike system.

3. Intermediate velocity source

The so-called intermediate velocity source exhibits a velocity roughly equal to half of the beam velocity for all light charged particles, regardless of the velocity bin considered. The value is equal to the nucleon-nucleon center of mass velocity and is in agreement with the systematics for reactions at intermediate energies [13,27,40,41].

The observed temperatures show a rather smooth increase as a function of $v_R/v_{\mathrm{c.m.}}$ ratio for protons, while alpha particle temperatures exhibit an almost flat behavior (Fig. 16). The need of a large slope parameter (or temperature parameter) for the intermediate source in three source moving fits is well documented [5,13,27,40]. Proton slope values observed as a function of the incident energy are well described by the relation valid for surface emission,

$$T=\frac{E_{\mathrm{beam}}}{8A_P}+6 \ \ \mathrm{MeV}, \tag{4}$$

where E_{beam} is the beam energy in MeV and A_P is the number of projectile nucleons. This estimate [5] arises from combined effect of the beam velocity and the Fermi motion on the energy of protons emitted following a single scattering between a projectile and a target nucleon. Equation (4) gives a temperature value of 10.6 MeV compared to $\simeq 11$ MeV obtained from the proton fits.

The proton multiplicity increases as a function of $v_R/v_{\mathrm{c.m.}}$, in agreement with a scenario in which the emitted protons come from first chance nucleon-nucleon collisions. Under this assumption, the increase of the multiplicity as a function of the residue velocity bins reflects the size of the interaction region; a similar trend was already observed at higher energies [40,42], and supports the idea of faster residues connected to more central collisions. A slight increase with residue velocity is also observed for the α particle multiplicity. However, the interpretation of the intermediate velocity source for α particle is rather controversial.

It seems clear that the intermediate velocity source stems from nonequilibrium particles emitted in the early stage of the reaction. More information on this stage should be provided by the study of high energy γ rays which is undertaken in Sec. V.

4. Momentum partition among sources

The multiple source scenario is undoubtedly a drastic simplification of the real reaction dynamics, but it can lead to an understanding of the momentum balance in the reaction and therefore to an estimation of the excitation energy of the primary composite nuclei which eventually de-excite through statistical emission of the light particles and γ rays. In order to infer the excitation energy transferred to the heavy residue, a procedure similar to that proposed in Ref. [27] was adopted, and applied to each of the residue velocity bins. Following this approach the excitation energy can be calculated estimating the initial momentum transfer assuming that all particles emitted from the projectilelike source

TABLE VI. The average momentum sharing among projectile, intermediate, and slow sources is shown in the first three columns. Columns 4 and 5 show the average mass carried away, respectively, by the projectile and intermediate velocity source. The contribution of the undetected mass to the total projectile mass together with the primary residue mass and its excitation energy calculated following the procedure described in the text are presented in the last three columns.

Velocity bin	$\langle P_{fast}/P_{tot}\rangle$	$\langle P_{int}/P_{tot}\rangle$	$\langle P_{slow}/P_{tot}\rangle$	M_{P-like}	M_{int}	ΔA	$\langle A\rangle$	E*
V37	0.60	0.11	0.29	21.5	8.5	12.5	104	280
V45	0.50	0.14	0.36	17.9	10.2	9.5	106	320
V55	0.43	0.15	0.42	15.5	11.1	7.5	107	340
V65	0.40	0.16	0.44	14.3	12.0	7.0	108	360
V73	0.35	0.16	0.49	12.5	12.3	5.5	109	390
V85	0.30	0.17	0.53	10.9	12.4	4.5	111	430
V93	0.26	0.17	0.57	9.5	12.7	3.5	111	460

are not contributing to the transfer, and then subtracting the contribution carried away by preequilibrium emission. The momentum removed by the projectilelike and intermediate velocity sources was estimated by affecting their respective source velocity to each of the particles emitted by these sources. The detection system used being blind to neutrons, it was assumed that for both sources the neutron and proton multiplicities are equal. This appears reasonable, as the ^{36}Ar projectile is an $N=Z$ nucleus.

Using momentum conservation, it is then possible to compute a velocity for the heavy recoiling fragment, which generally turns out to be larger than the velocity of the slow source extracted from the moving source fit. This discrepancy is attributed to the existence of a beam velocity projectile fragment which would not be detected by the experimental setup. The mass of this fragment appears to decrease with increasing centrality, going from $A=12.5$ for the most peripheral reactions to $A=3.5$ for the most central reactions in agreement with a reaction mechanism proceeding through an incomplete fusion scenario.

Assuming that the procedure outlined above accounts for the bulk of the mass which is not transferred to the heavy recoiling fragment, it is then possible to estimate the average excitation energy and mass of the primary residue before statistical decay for each velocity bin and to follow the evolution of the momentum sharing (and energy sharing) among sources as a function of the centrality of the reaction. The results of this analysis are given in Table VI. The average number of projectile-like nucleons not contributing to the momentum transfer increases from 9.5 for the highest velocity bin to 21.5 amu for the bin associated to the lowest transfers. These numbers include the contribution of the unobserved fragment mass which increase from a value of about 3.5 amu to about 12.5 amu. This might be an indication that for low transfers the missing mass and momentum are mainly carried away by a large fragment.

The average number of nucleons emitted by the intermediate source (pre-equilibrium emission) ranges from 8.5 to 12.7. The associated momentum removed by this source ranges from 11% to 17% of the total momentum and therefore it gives a non-negligible contribution in lowering the excitation energy and mass of the compound system formed in the reaction.

D. Characteristics of the fusionlike source

The approach described above allows us to estimate an average mass of the heavy recoil at the end of the preequilibrium emission phase. From momentum and mass conservation it follows that the mass of the recoil increases with momentum transfer from 104 amu to 111 amu (see Table VI). At the same time the excitation energy of the system increases from 280 MeV up to 460 MeV, showing that highly excited nuclei are produced in events associated with the largest momentum transfers.

The independent measure of the excitation energy and temperature of the system, respectively from momentum and energy conservation considerations and fit of alpha particle spectra for all velocity bins, allows a comparison of the trend of our data with respect to the predictions of the Fermi gas formula $E=aT^2$, where $a=A/K$ is the level density param-

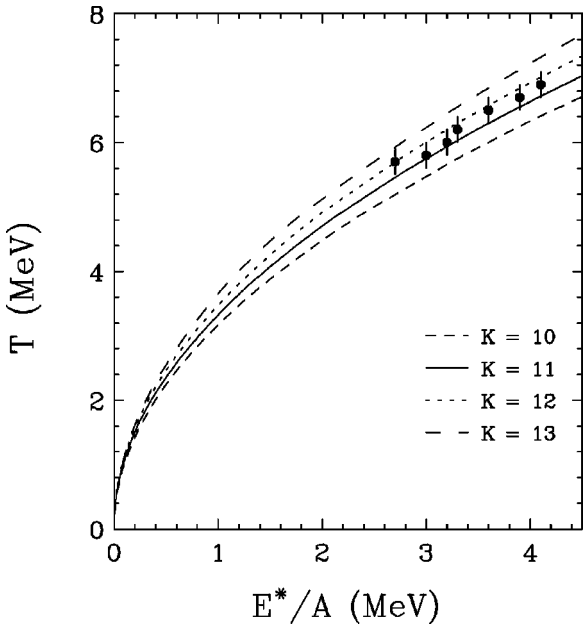

FIG. 17. Temperature of the primary residue as a function of its excitation energy per nucleon. Full symbols are experimental data while the different curves show the Fermi gas estimate for the correlation between the two variables using different level density parameter $a=A/K$, with K ranging from $K=10$ to 13 MeV.

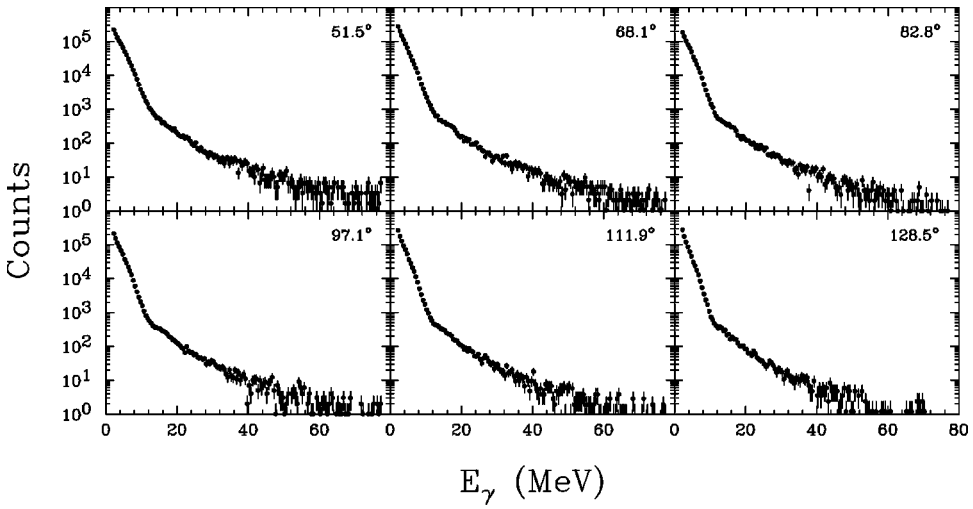

FIG. 18. Gamma spectra detected at different angles in the laboratory frame in coincidence with residues having an average velocity equal to 65% of the c.m. velocity.

eter. In Fig. 17 the temperature of the system extracted from the fit of alpha particle spectra is shown as a function of E^*/A. The different lines represent the prediction of the Fermi gas formula for different values of K ranging from $K=10$ to 13 MeV. All data points are enclosed between $K=11$ and 12 MeV, confirming a theoretical calculation which predict an increase of the level density parameter from $K=8.5$ MeV at zero temperature to $K=12$ MeV above $T=5$ MeV for nuclei in the $A=110$ mass region [43]. The trend observed has been compared with a recent work on the caloric curves where temperature extracted using slope of particle spectra and double isotope yield ratio are compared for different reactions [44]. The effect of a mass dependence on the caloric curve is also investigated, and conclusions are drawn concerning limiting temperatures and excitations energies at which a departure from the Fermi gas trend sets in and a flattening is observed. The caloric curve extracted in our work is in good agreement with systematics shown in the paper for excitation energies between 2.7 and 4.1 MeV/nucleon. Indeed, in this mass region, the systematics show evidence for limiting temperature of about 7 MeV, and a departure from the Fermi gas trend for energies above 4 MeV/nucleon and therefore above the excitation energy range investigated in this paper.

IV. GAMMA RAY SPECTRA

A. Raw data

Gamma ray spectra have been measured with the BaF_2 detectors in the angular range between 42° and 170°, in coincidence with fusionlike residues. The data have been sorted according to the previously described velocity bins used for the charged particle analysis. As an example, γ-ray spectra measured at different angles in coincidence with fusionlike residues, belonging to the 65% center of mass velocity bin are presented in Fig. 18. These spectra can be qualitatively understood as being composed of three components of different origin. The low energy range ($E_\gamma < 10$ MeV) can be explained in terms of emission from the compound nucleus at the end of the deexcitation process, which gives rise to a steep exponential component with inverse slopes of the order of 1.5–2 MeV. This statistical component is almost independent of the initial excitation energy and mass of the compound nucleus. At high energy ($E_\gamma > 35$ MeV) an exponentially decreasing component, with inverse slope values of the order of 10 MeV, extends to very high energies. The commonly accepted explanation of this component is in terms of nucleon-nucleon bremsstrahlung originating during the initial stages of the reaction [16]. In the range $E_\gamma = 10$–20 MeV, γ rays from the decay of the giant dipole resonance excited in the fusionlike nuclei give rise to a characteristic bump in the spectrum [26,45] centered at about 15 MeV. This value is consistent with an emission from an excited nucleus of mass ≈ 110.

Comparing the spectral shape at different angles (Fig. 18) it can be noted that, while the low energy statistical contribution shows slight differences due to Doppler shift effects as a function of the detection angle, the high energy component exhibits a sharp dependence on the detection angle, becoming steeper with increasing polar angle. This trend, already observed in previous experiments, suggests an emission from a fast moving source.

In the following we will concentrate on the high energy component. In order to study the origin of this component the spectra were normalized to the number of fusionlike residue events for each bin. This number was deduced from a minimum bias run where only the PPAC triggered the acquisition system by using the integrated beam current measured in the Faraday cup and taking into account the overall dead time.

Event selection based on residue velocity allows the study of the evolution of the gamma multiplicity, the inverse slope parameter and to search for any variation in the emitting source velocity as a function of the ratio $v_R/v_{\mathrm{c.m.}}$.

B. Unfolding of the experimental photon spectra

The experimental photon spectra are related to the hard photon cross section by

$$\frac{d^2N}{d\Omega dE_d} = C\int_0^\infty R(E_\gamma, E_d)\frac{d^2\sigma}{d\Omega dE_\gamma}dE_\gamma \qquad (5)$$

where C is a normalizing factor and $R(E_\gamma,E_d)$, the response function of the BaF_2 detectors, expresses the probability that the electromagnetic shower associated to an incident photon with energy E_γ deposits the energy E_d into the crystal. The response $R(E_\gamma,E_d)$ in the 20–280-MeV range was measured with collimated monochromatic photons [46]. The double differential cross section $d^2\sigma/d\Omega dE_\gamma$ was determined from Eq. 5 at the various detection angles by the unfolding method tested in Refs. [47,48]. The method performs a simultaneous data correction for the BaF_2 detection efficiency as well as for the deposited energy to incident energy conversion. The error of the unfolding procedure was estimated as in Refs. [47,48].

C. Analysis of the bremsstrahlung component

Assuming an emission from a source moving with a velocity β, emitted spectra in the source reference frame are connected (because of Doppler effect) to the laboratory ones through the relations

$$E_{lab}=E_s\frac{(1+\beta\cos\theta_s)}{\sqrt{1-\beta^2}}, \tag{6}$$

$$\sin\theta_s=\sin\theta_{lab}\frac{\sqrt{1-\beta^2}}{(1-\beta\cos\theta_{lab})}=\frac{\sin\theta_{lab}}{X}, \tag{7}$$

$$\frac{d^2\sigma(\theta_{lab},E_{lab})}{d\Omega_{lab}dE_{lab}}=\frac{1}{X}\frac{d^2\sigma(\theta_s,E_s)}{d\Omega_s dE_s}, \tag{8}$$

where E_{lab} and E_s are, respectively, the gamma energy in the laboratory reference frame and in the source frame, θ_{lab} and θ_s are the detection angle and the emission angle in the source reference frame and X is given by

$$X=\frac{(1-\beta\cos\theta_{lab})}{\sqrt{1-\beta^2}}=\gamma(1-\beta\cos\theta_{lab}). \tag{9}$$

Considering a non isotropic source emitting γ rays giving rise to an exponential spectrum as

$$\frac{d^2\sigma(\theta_s,E_s)}{d\Omega_s dE_s}=f(\sin\theta_s)\exp\left(-\frac{E_s}{E_0}\right), \tag{10}$$

the observed spectrum in the lab. frame will be given by

$$\frac{d^2\sigma(\theta_{lab},E_{lab})}{d\Omega_{lab}dE_{lab}}=\frac{1}{X}\exp\left(-\frac{E_{lab}\gamma(1-\beta\cos\theta_{lab})}{E_0}\right)f\left(\frac{\sin\theta_{lab}}{X}\right). \tag{11}$$

In such a relation, to each detection angle corresponds an exponential spectrum with an angle dependent inverse slope

$$E_0'=E_0\frac{\sqrt{1-\beta^2}}{(1-\beta\cos\theta_{lab})}, \tag{12}$$

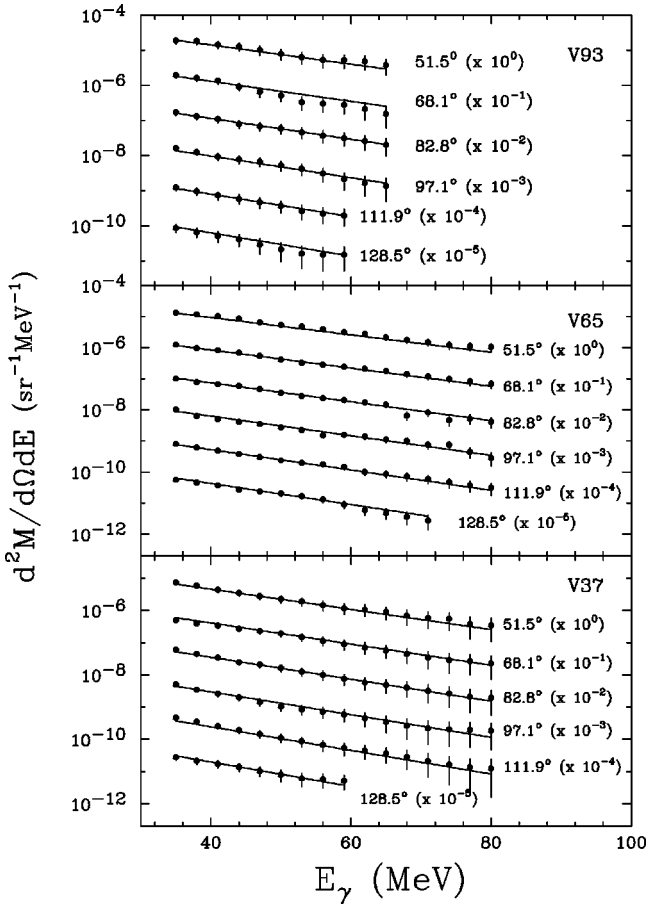

FIG. 19. High-energy gamma spectra detected at different angles in the laboratory frame in coincidence with residues having an average velocity equal to 93% (top), 65% (middle), and 37% (bottom) of the c.m. velocity. Full lines represent the fits to the data.

which gives a description consistent with the experimental data of Fig. 18. Assuming an angular distribution in the source reference frame given by a superposition of an isotropic and a dipole component, the distribution can be written as

$$f(\sin\theta_s)=1-\alpha(1-\sin^2\theta_s). \tag{13}$$

Putting this relation in the differential cross section formula yields

$$\left[\frac{d^2\sigma}{d\Omega dE_\gamma}\right]_{lab}=\frac{K}{X}\left(1-\alpha+\alpha\frac{\sin^2\theta_{lab}}{X^2}\right)\exp\left(-X\frac{E_{lab}}{E_0}\right), \tag{14}$$

where K is the cross section in the source reference frame.

The high energy part of the γ spectra, namely, $E_\gamma\geqslant 35$, shown in Fig. 19 has been analyzed with a simultaneous fit procedure using Eq. (14). The inverse slope and the source velocity have been deduced from the fit. Because of the limited statistics it was not possible to extract a reliable value for the dipole fraction α. Therefore, the factor α was fixed to 0.2 according to the known systematics [16]. The results as a function of the different residue recoil velocities are shown

TABLE VII. Inverse slope and source velocity extracted from a simultaneous fit of the high energy part of the gamma spectra ($E_\gamma \geqslant 35$ MeV).

Velocity bin	$v_R/v_{\text{c.m.}}$	E_0 (MeV)	v_s/c
V37	0.37	12.2 ± 0.9	0.15 ± 0.01
V45	0.45	13.0 ± 0.8	0.15 ± 0.01
V55	0.55	13.6 ± 0.7	0.15 ± 0.01
V65	0.65	14.0 ± 0.8	0.15 ± 0.01
V73	0.73	14.3 ± 0.9	0.15 ± 0.01
V85	0.85	14.5 ± 0.9	0.15 ± 0.01
V93	0.93	14.5 ± 1.0	0.15 ± 0.01

in Table VII. Uncertainties on the parameter values correspond to the change in a parameter that increases χ^2 by 1, with all the other parameters fixed at their optimum values [31]. Fit results as a function of the velocity bins give a good description of the data in terms of a single source having a constant velocity ($\beta=0.15$) close to half beam velocity ($\beta=0.14$), in agreement with the systematics [16]. This velocity has to be compared with the residue velocity which ranges from $\beta=0.030$ to $\beta=0.052$ with increasing centrality. This shows that the high energy γ rays do not originate from the slow moving thermal source.

Considering the error bars the inverse slope parameter is almost independent of recoil velocity, even if a slight increase can be inferred (Fig. 20) for the most central collisions. Such an evolution has been observed in other exclusive experiments and, in the framework of incoherent np bremsstrahlung, has been interpreted as due to the softening of the nucleon Fermi momentum distribution at the nuclear surface [19].

V. PROBES OF THE PRE-EQUILIBRIUM PHASE: HARD PHOTONS AND HIGH ENERGY PROTONS

Studies on high energy γ-ray and energetic proton production have shown, in both cases, remarkably similar behaviors. Both originate from sources with velocity close to half the beam velocity and both exhibit spectra with high inverse slope values. Moreover the multiplicity of both high energy protons [40] and photons [18,19] increases with decreasing impact parameter, reflecting the size of the participant region. These similarities indicate that both high energy protons and high energy gamma rays originate from the same mechanism, namely, the nucleon-nucleon collisions in the first stage of the reaction.

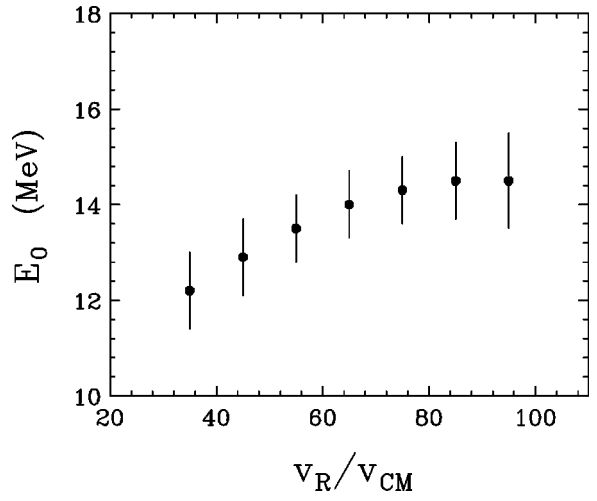

FIG. 20. Inverse slope parameter, as obtained from the fit, as a function the ratio $v_R/v_{\text{c.m.}}$.

A. Hard photon–high energy proton correlations

In order to verify the hypothesis of hard photon and high energy proton emission from the first chance nucleon-nucleon collisions we have investigated the correlation between the most energetic protons and γ rays, similarly to what has been described by Sapienza *et al.* in Ref. [19]. Differently from the previous work, the existence of correlation is investigated here for events in which fusion-like residues are formed. In the frame of the first chance pn incoherent bremsstrahlung model an anticorrelation effect between the emission of a hard photon and an energetic pre-equilibrium proton is expected [49]. This effect is determined by the conservation of the energy in the individual pn collision, which in the case of hard photon emission imposes a stronger constraint: when the two nucleons have a sufficiently high relative momentum so that a high energy photon is emitted as a consequence of the collision the scattered proton has a reduced energy in accordance with the energy conservation law. In the case of statistical emission from an excited system or independent proton and high-energy γ-ray emission the anticorrelation is expected to be washed out due to the higher available energy in the composite system.

In order to study the high energy γ-proton correlation the hard γ-p correlation factor was introduced [19,50] as

$$1+R_{\gamma p}=\frac{\langle m_p\rangle_\gamma}{\langle m_p\rangle} \tag{15}$$

where $\langle m_p\rangle$ and $\langle m_p\rangle_\gamma$ are the average proton multiplicity and the average proton multiplicity measured in coincidence with the hard photon, respectively. The correlation factor plotted as a function of the proton energy reflects just the difference between the proton energy spectrum in coincidence with the photon and the inclusive proton spectrum. In the case of statistical photon emission, where no correlation is expected, a value of the correlation factor very close to 1 should be observed irrespectively of the proton energy. Anticorrelation effects will lead to values of $1+R_{\gamma p}<1$.

The γ-proton anticorrelation is expected only for pre-equilibrium protons, and protons from projectilelike source should be excluded. The moving sources analysis of proton spectra suggests that at laboratory angles larger than 42° and above an energy of 40 MeV the contribution to the proton yield coming from the intermediate source is about 90% of the total yield. Therefore, only those protons were retained in the analysis. The experimental correlation function $1+R_{\gamma p}(E_p)$ for hard photons with energy higher than 25 and 70 MeV are reported versus the proton energy E_p in Fig. 21

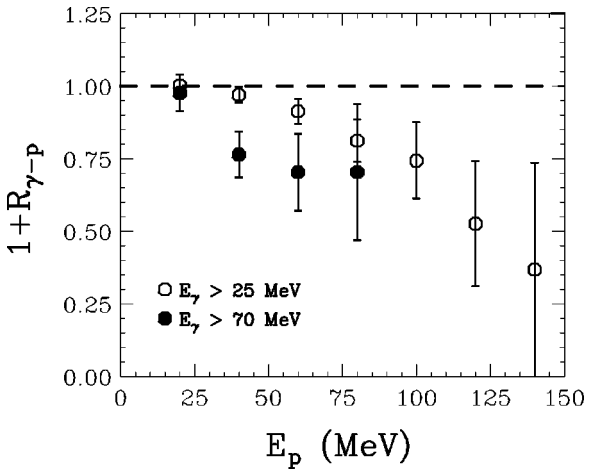

FIG. 21. Hard photon–high energy proton correlation function for $E_\gamma \geqslant 25$ MeV (open symbols) and for $E_\gamma \geqslant 70$ MeV (full symbols).

for the central and mid-central collisions ($v_R/v_{\mathrm{c.m.}} > 0.5$). The experimental γ-p correlation function is found to be smaller than 1 for both γ energy thresholds, with a more pronounced decreasing trend for the data set selected choosing $E_\gamma > 70$ MeV. The observation of the strong $\gamma - p$ correlation in events triggered by fusionlike residues indicates that even if one reaction leads to the formation of a composite system, with the damping of a large fraction of incident energy in excitation energy, the hard photons and energetic protons emission mainly occurs during the initial phase of the reaction as a consequence of nucleon-nucleon collisions.

B. Hard photon multiplicity—recoil velocity correlation

Throughout this study, the recoil velocity $v_R/v_{\mathrm{c.m.}}$ of the residue has been used as an event selector. The evolution of many parameters such as the multiplicity of fast protons and the temperature and multiplicity of the slow source implies that $v_R/v_{\mathrm{c.m.}}$ is correlated with the centrality of the collision. Here, using the hard γ multiplicity, we will demonstrate the correlation in a more direct way. This analysis was already presented elsewhere [51], and in that case was used in comparison with a similar system at lower incident energy to elucidate the role of two body collisions in the dissipation mechanism.

Since high energy γ rays are mostly produced in first chance pn collisions in the early stage of the reaction, they represent a direct tool to determine the collision impact parameter since their multiplicity reflects the size of the interaction region and is thus directly related to the impact parameter [18]. The relation between the hard photon multiplicity and the impact parameter was confirmed by the measurement of correlations between hard photons and light charged particle multiplicities which are also known to be an indicator of the centrality of the collision [18–20]. In the hypothesis of production by incoherent bremsstrahlung radiation through pn collisions the multiplicity of the high energy γ rays scales with the number of individual first chance pn collisions that occur in the geometrical overlap

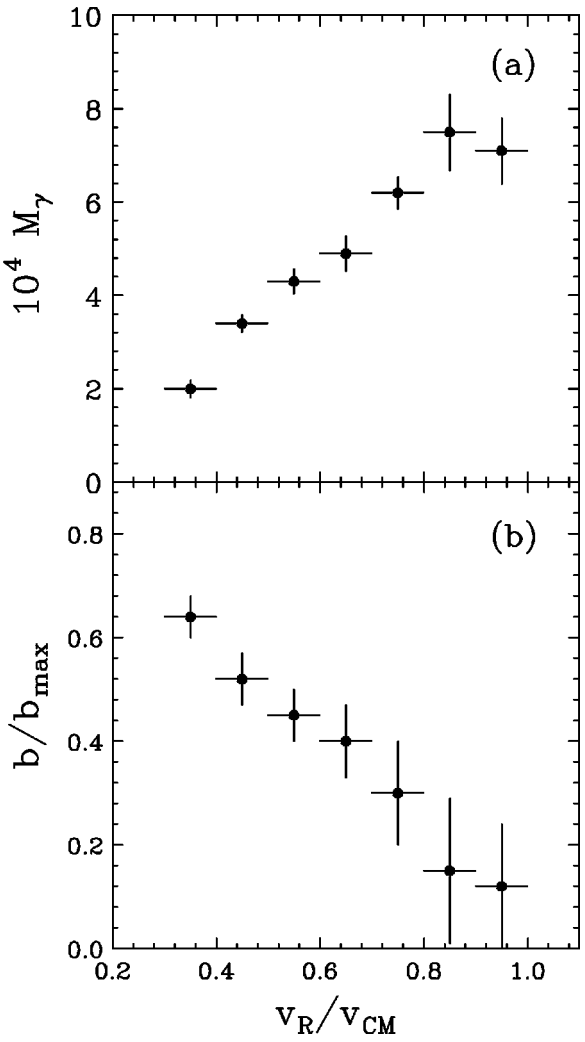

FIG. 22. (a) Multiplicity of γ rays with $E_\gamma > 35$ MeV as a function of $v_R/v_{\mathrm{c.m.}}$. (b) impact parameter dependence of γ rays as a function of momentum transfer $v_R/v_{\mathrm{c.m.}}$.

region. Assuming that the probability P_γ of producing a photon in a single pn collision depends only on the beam energy, the gamma ray multiplicity for a given impact parameter $M_\gamma(b)$ is related to the number $N_{pn}(b)$ of first chance pn collisions by the relation [16]

$$M_\gamma(b) = N_{pn}(b) P_\gamma, \tag{16}$$

where one assumes a P_γ independent of the impact parameter. Since the photon production probability per single pn collision at these bombarding energies is of the order of 10^{-5}, high energy γ rays cannot be used to deduce N_{pn} on an event-by-event basis. However, an average value can still be deduced for a class of events selected by another observable, such as the recoil velocity in our case, and can help to classify these events in terms of their average impact parameter [21].

The high energy γ-ray multiplicity M_γ was determined for each residue velocity bin by normalizing over 4π the γ-ray yield measured around 90° integrated above 35 MeV. In Fig. 22(a) multiplicity values are shown as a function of

$v_R/v_{\mathrm{c.m.}}$. A strong and linear increase as a function of recoil velocity is observed showing the important role of two body dissipation mechanisms for the momentum transfer. The information concerning the average impact parameter per velocity bin was deduced from the hard photon multiplicity. Using Eq. (16) the number of pn collisions can be calculated for all the velocity bins once the P_γ is known. The value of $P_{\gamma>35}$ was determined from the minimum bias run to be $(4.0\pm0.6)\times10^{-5}$ using $P_\gamma=\sigma_\gamma/(\langle N_{pn}\rangle_b\sigma_R)$, where σ_γ and σ_R are the measured hard γ-ray production cross section and the total reaction cross section, and $\langle N_{pn}\rangle_b$ is the number of pn collisions averaged over the impact parameter. Then, applying the geometrical model [16], the average impact parameter was deduced from $N_{np}(b)$. Figure 22(b) shows the measured reduced recoil velocity as a function of the reduced impact parameter $b/b_{\max}$ where the $b_{\max}$ value was calculated as $b_{\max}=1.2(A_P^{1/3}+A_T^{1/3})=9.5$ fm, A_P and A_T being the projectile and target masses.

The strong correlation previously observed in Fig. 22(a) remains between the recoil velocity and the impact parameter [Fig. 22(b)] showing that the fraction of linear momentum transfer is strongly correlated with the impact parameter confirming that the most central collisions give rise to the largest transfers to the targetlike nucleus [51]. This correlation will be helpful in comparing our results with dynamical models which furnish predictions as a function of the impact parameter.

VI. COMPARISON WITH DYNAMICAL MODELS

Reliable information about the reaction mechanisms involved in heavy ion collisions at intermediate energies can be obtained in the framework of one-body transport theories. The Landau-Vlasov (LV) [52], Boltzmann-Uehling-Uhlenbeck (BUU) [53], or Boltzmann-Nordheim-Vlasov (BNV) [53–56] transport equation, which describes the time evolution of the nucleon one-body distribution function in phase space, $f(\vec{r},\vec{p},t)$, provides a generally good average description of the dissipative mechanisms occurring all along the interaction between the two colliding nuclei. Depending on entrance channel properties, namely the impact parameter, the beam energy, and the mass asymmetry, different outgoing channels, ranging from the formation of only one composite nuclear source, in the case of central collisions, up to deep-inelastic-like collisions or inc omplete fusion processes, for more peripheral reactions, are observed. In such a context, in this section we will try to obtain a deeper insight into the reaction mechanisms which could be responsible for the light particle and γ-ray emission observed in the ^{36}Ar+^{98}Mo reaction at 37*A* MeV.

In one-body transport theories the time evolution of the distribution function $f(\vec{r},\vec{p},t)$ is ruled by the action of a mean-field potential, together with the effect of a Pauli-blocked collision term, according to the equation

$$\frac{\partial f(\vec{r},\vec{p},t)}{\partial t}+\{f(\vec{r},\vec{p},t),H\}=I_{coll}[f(\vec{r},\vec{p},t)], \qquad (17)$$

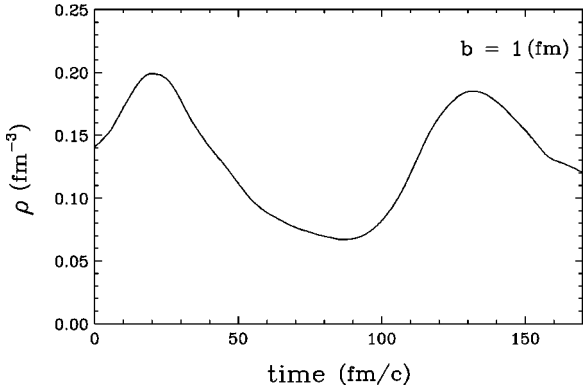

FIG. 23. Time evolution of the central density calculated at impact parameter $b=1$ fm.

where $\{,\}$ stands for the Poisson bracket, H is the self-consistent one-body Hamiltonian and I_{coll} is the Uehling-Uhlenbeck collision term. In the following calculations a Skyrme-like parametrization is used for the description of the mean-field potential, which gives a ''soft'' equation of state, with a compressibility modulus $K=200$ MeV,

$$U(\rho)=A(\rho/\rho_0)+B(\rho/\rho_0)^\sigma, \qquad (18)$$

with $A=-356$ MeV, $B=303$ MeV, and $\sigma=7/6$. Equation (17) is solved numerically, according to the test particle method, with the code TWINGO [55], using 200 test particles per nucleon.

Simulations have been performed for impact parameters ranging from 0 to 7 fm. At these bombarding energies, for central reactions, the density of the system evolves through a first initial compression phase to an expansion phase, after roughly 50 fm/c (see Fig. 23) but since the internal pressure is not sufficient to break the system into fragments after some expansion it reverses to compression leading to the formation of a heavy system (see Fig. 23). For small impact parameters ($b<2$ fm), for which the target completely overlaps the projectile, a mechanism akin to incomplete fusion with the formation of a single heavy source is observed as it can be seen in Fig. 24 where the contour plots of the evolution of the spatial density as a function of time in the case of a reaction at $b=0$ fm are shown. At larger impact parameters the outgoing channel is essentially binary as can be seen in Fig. 24 where similar calculations for b = 3 and 6 fm are shown and the pseudo-particles appear located in two main regions in $\vec{r}$ space, which can be associated, respectively, with the projectilelike (PLF) and targetlike (TLF) fragments. However, from an analysis in $\vec{p}$ space, it is also possible to recognize a component located around the nucleon-nucleon center of mass velocity region which can be associated to the pre-equilibrium emission corresponding to particles emitted by the system mostly during the first 120 fm/c. The presence of pre-equilibrium particle emission can be more clearly observed in Fig. 25(a) where the number of emitted particles as a function of time is shown for collisions at $b=1$ fm. The slope change in the production rate at about 120–140 fm/c indicates a transition from preequilibrium to the evaporation from equilibrated sources [54]. At this time already a large

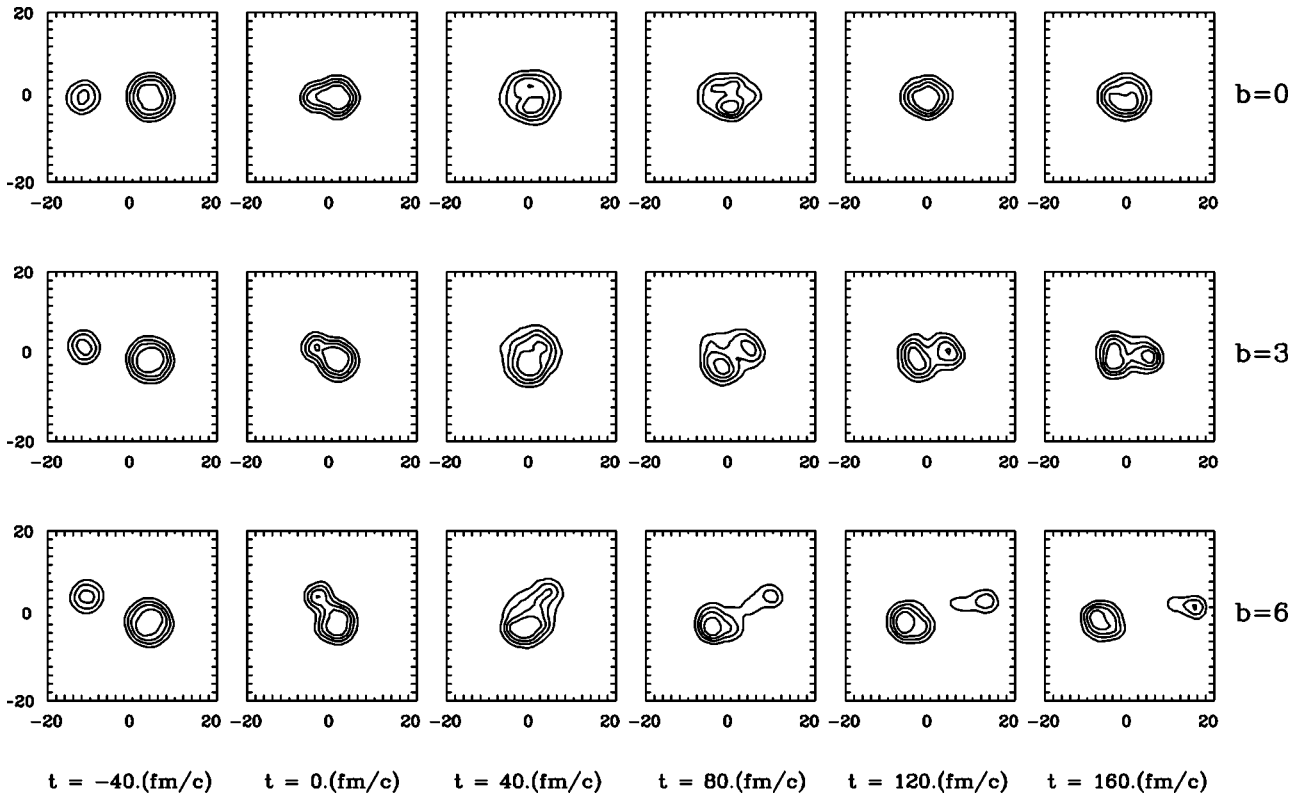

FIG. 24. Contour plots of the spatial density as a function of time in the reaction plane for different impact parameters: $b=0$ fm (top), $b=3$ fm (middle), and $b=6$ fm (bottom).

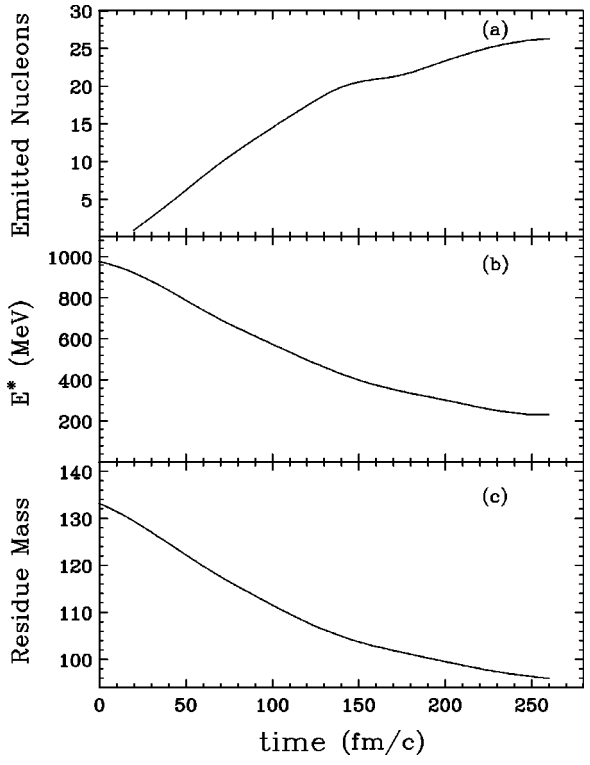

FIG. 25. (a) Number of emitted nucleons during the reaction as a function of time. (b) Excitation energy of the heavy residue as a function of time obtained at $b=1$ fm. (c) mass of the heavy residue as a function of time calculated at $b=1$ fm.

amount of particles has been emitted. This affects the excitation energy of the system since preequilibrium emission removes a large amount of the energy from the system, leaving the primary source with moderate excitation energies and a lower mass [see Figs. 25(b) and 25(c)]. The collision scenario predicted by the BNV calculation exhibits many similarities with that inferred from the empirical moving source fit. In particular, one can associate the slow, fast and intermediate velocity sources introduced by the fit to the data with emission from excited target and projectilelike fragments and preequilibrium emission respectively.

In order to proceed further, it is therefore informative to compare the properties of the sources predicted by the calculation with those extracted from the fits. In the top panel of Fig. 26 the velocity of the targetlike source is presented as a function of the reduced impart parameter ($b/b_{\max}$). The full line represents the BNV calculation while symbols are the experimental data. The velocity of the heavy residue as calculated from BNV is larger than the one obtained from the fit of alpha particle spectra at all impact parameters. In the same figure is also shown, as a comparison, the average velocity of the residue measured in each bin deduced from time of flight between the target and the PPAC. This direct measurement of the heavy residue velocity is again lower than what is predicted by BNV calculation even if, approaching the most central collisions, the difference is much reduced. This discrepancy could be due to the lack of fluctuations in our mean-field description of the dynamical evolution of the system. As a consequence, the time needed for the dinuclear

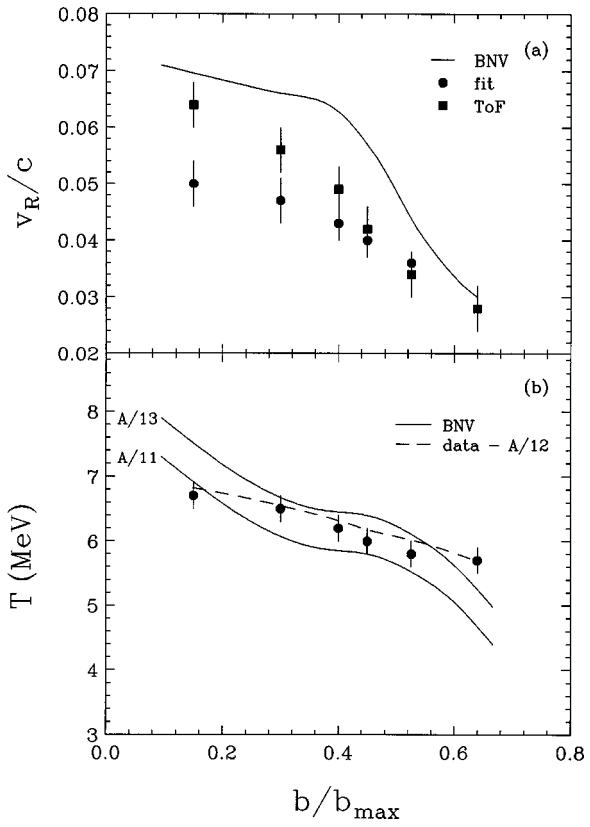

FIG. 26. The properties of the heavy source formed in the reaction as a function of the reduced impact parameter. (a) Comparison of the heavy source velocity obtained from the BNV calculation (full line) with the velocities deduced from the fit of alpha particle spectra (full circles) and from time of flight measurement (full squares). (b) Comparison of the temperature extracted from the alpha particle specta (full circles) with temperatures deduced from BNV calculations (full lines) using level density parameters $A/11$ MeV^{-1} and $A/13$ MeV^{-1}, and those estimated from the reconstructed excitation energy using a level density parameter $A/12$ MeV^{-1} (dashed line).

system to break-up into PLF- and TLF-like fragments is too long, leading to velocities closer to the center of mass velocity.

Apparent temperatures extracted from the fit of alpha particles and temperatures deduced from BNV calculations are shown in the lower panel of Fig. 26 as a function of the collision centrality. The temperature values obtained from BNV calculation, shown as full lines, were deduced from the calculated excitation energies assuming level density parameter ranging from $A/11$ MeV^{-1} and $A/13$ MeV^{-1}. The BNV temperatures are in agreement with the temperatures extracted from the fits using level density parameters in the range $A/11$–$A/12$ MeV^{-1}. It should be recalled, however, that although the initial temperatures are surely higher than the apparent temperatures extracted from the alpha particle spectra and shown above, the value of the empirical coefficients to be used at this bombarding energy might differ from those extracted in Ref. [39] for reactions at lower energy. Moreover, BNV temperature values suffer from uncertainties due to the time when the excitation energy is calculated. This has been fixed in the BNV simulation at the time when preequilibrium emission is finished. Decreasing this time slightly would result in a marked increase of the excitation energy. As a further term of comparison the values of the excitation energy of the primary residue reconstructed with the procedure presented in Sec. III D were used to extract the temperature of the residue adopting a level density parameter $A/12$ MeV^{-1}. The result is shown as a dashed line in the lower panel of Fig. 26 and is in very good agreement with the temperature extracted from alpha particle spectra giving a further evidence of the consistency of the scenario with a level density between $A/11$ and $A/12$ MeV^{-1}.

In conclusion, the BNV calculation paints a picture of the reaction process in agreement with that inferred from the charged particle and γ-ray measurements. More quantitative comparisons are plagued by the uncertainty concerning the time at which the relevant observables must be calculated in the simulation, and by the use of the moving source picture for the analysis of the experimental data. Progress could be made if charged particles and γ-ray spectra could be directly extracted from the calculation and compared to the raw measured data.

VII. CONCLUSIONS

In this experiment the reaction ^{36}Ar+^{98}Mo at 37A MeV was studied through an analysis of high energy gamma rays and light charged particles detected in coincidence with evaporation residues. The reaction products were sorted as a function of the linear momentum transferred to the heavy residue produced in the reaction. Through the use of different probes the evolution of the reaction dynamics from the preequilibrium stage to the formation of a heavy compound nucleus was investigated.

The study of light charged particle spectra performed through a moving source fit with three sources indicates the formation of a highly excited system with temperature of about 7 MeV and the existence of a copious preequilibrium emission. The independent measurement of excitation energy of the primary residue and temperature allowed a close comparison with the prediction of the Fermi gas formula suggesting a value of the level density parameter between $A/11$ and $A/12$ MeV^{-1}. The preequilibrium emission was investigated in detail through the study of high energy ($E_\gamma > 35$ MeV) γ rays and high energy protons. The multiplicity of high energy γ rays was found to increase with the linear momentum transfer, giving one a tool to correlate the momentum transfer with the impact parameter. The study of the correlation between the most energetic photons and protons allowed us to obtain a further experimental evidence of their common origin confirming the hypothesis of a production from the most energetic primary nucleon-nucleon collisions.

In an attempt to get a deeper comprehension of the reaction mechanism the experimental findings were compared to BNV calculations. The results obtained from the BNV reproduce the average findings concerning the formation of a residue and suggest a larger dissipation than the one deduced from the analysis of light charged particle and high energy

γ-ray spectra. A reaction scenario can be inferred from the above findings. The interaction starts with nucleon-nucleon collisions in the region of overlap of the nuclear densities. These collisions give rise to the production of high energy nucleons and γ rays, and are also instrumental in driving the transfer of energy from relative motion to internal excitation of both target and projectile entities. In the present case a strongly excited target-like fragment and a modestly excited projectilelike fragment are produced, which subsequently decay by particle and finally statistical γ-ray emission. The trigger of the present experiment, i.e., the presence of a large evaporation residue, precluded the observation of energy transfer large enough to result in the multifragmentation of the system.

[1] R. Lacey, N.N. Ajitanand, J.M. Alexander, D.M. de Castro Rizzo, G.F. Peaslee, L.C. Vaz, M. Kaplan, M. Kildir, G. La Rana, D.J. Moses, W.E. Parker, D. Logan, M.S. Zisman, P. De Young, and L. Kowalski, Phys. Rev. C **37**, 2561 (1988).

[2] J. Boger, J.M. Alexander, R.A. Lacey, and A. Narayanan, Phys. Rev. C **49**, 1587 (1994).

[3] L.C. Moretto and G.J. Wozniak, Annu. Rev. Nucl. Part. Sci. **34**, 189 (1984).

[4] E. Suraud, C. Gregoire, and B. Tamain, Prog. Part. Nucl. Phys. **23**, 357 (1989), and references therein.

[5] H. Fuchs and K. Möhring, Rep. Prog. Phys. **57**, 231 (1994).

[6] H. Morgestern, W. Bohne, K. Grabisch, D.G. Kovar, and H. Lehr, Phys. Lett. **113B**, 463 (1882).

[7] V.E. Viola Jr., B.B. Back, K.L. Wolf, T.C. Awes, C.K. Gelbke, and H. Breuer, Phys. Rev. C **26**, 178 (1982).

[8] C.J. Gelderloos, J.M. Alexander, J. Boger, M.T. Magda, A. Narayanan, P. DeYokung, A. Elmaani, and M.A. McMahan, Phys. Rev. C **54**, 3056 (1996).

[9] K. Hanold, L.G. Moretto, G.F. Peaslee, G.J. Wozniak, D.R. Bowman, M.F. Mohar, and D.J. Morrissey, Phys. Rev. C **48**, 723 (1993).

[10] K.A. Hanold, D. Bazin, M.F. Mohar, L.G. Moretto, D.J. Morrissey, N.A. Orr, B.M. Sherrill, J.A. Winger, G.J. Wozniak, and S.J. Yennello, Phys. Rev. C **52**, 1462 (1995).

[11] M.T. Magda, E. Bauge, A. Elmaani, T. Braunstein, C.J. Gelderloos, N.N. Ajitanand, John M. Alexander, T. Ethvignot, P. Bier, L. Kowalski, P. Désequelles, H. Elhage, A. Giorni, S. Kox, A. Lleres, F. Merchez, C. Morand, P. Stassi, J.B. Benrachi, B. Chambon, B. Cheynis, D. Drain, and C. Pastor, Phys. Rev. C **53**, R1473 (1996).

[12] M. Gonin, J.P. Coffin, G. Guillaume, F. Jundt, P. Wagner, P. Fintz, B. Heusch, A. Malki, A. Fahli, S. Kox, F. Merchez, and J. Mistretta, Phys. Rev. C **38**, 135 (1988).

[13] R. Wada, D. Fabris, K. Hagel, G. Nebbia, Y. Lou, M. Gonin, J.B. Natowitz, R. Billerey, B. Cheynis, A. Demeyer, D. Drain, D. Guinet, C. Pastor, L. Vagneron, K. Zaid, J. Alarja, A. Giorni, D. Heuer, C. Morand, J.B. Viano, C. Mazur, C. Ngô, S. Leray, R. Lucas, M. Ribrag, and E. Tomasi, Phys. Rev. C **39**, 497 (1989).

[14] M.T. Magda, T. Ethvignot, A. Elmaani, J.M. Alexander, P. Desesquelles, H. Elhage, A. Giorni, D. Heuer, S. Kox, A. Lleres, F. Merchez, C. Morand, D. Rebreyend, P. Stassi, J.B. Viano, F. Benrachi, B. Chambon, B. Cheynis, D. Drain, and C. Pastor, Phys. Rev. C **45**, 1209 (1992).

[15] T. Ethvignot, N.N. Ajitanand, J.M. Alexander, A. Elmaani, C.J. Gelderloos, P. Désesquelles, H. Elhage, A. Giorni, D. Heuer, S. Kox, A. Lleres, F. Merchez, C. Morand, D. Rebreyend, P. Stassi, J.B. Viano, F. Benrachi, B. Chambon, B. Cheynis, D. Drain, and C. Pastor, Phys. Rev. C **47**, 2099 (1993).

[16] H. Nifenecker and J.A. Pinston, Annu. Rev. Nucl. Part. Sci. **40**, 113 (1990).

[17] W. Cassing, V. Metag, U. Mosel, and K. Niita, Phys. Rep. **188**, 365 (1990).

[18] E. Migneco, C. Agodi, R. Alba, G. Bellia, R. Coniglione, A. Del Zoppo, P. Finocchiaro, C. Maiolino, P. Piattelli, G. Russo, P. Sapienza, A. Badalá, R. Barbera, A. Palmeri, G.S. Pappalardo, F. Riggi, A.C. Russo, A. Peghaire, and A. Bonasera, Phys. Lett. B **298**, 46 (1993).

[19] P. Sapienza, R. Coniglione, R. Alba, A. Del Zoppo, E. Migneco, C. Agodi, G. Bellia, P. Finocchiaro, K. Loukachine, C. Maiolino, A. Peghaire, P. Piattelli, and D. Santonocito, Phys. Rev. Lett. **73**, 1769 (1994).

[20] G. Martinez, J. Diaz, M. Franke, S. Hlavac, R. Holzmann, P. Lautridou, F. Lefebre, H. Lohner, A. Marin, M. Marques, T. Matulewitz, W. Mittig, R.W. Ostendorf, J.H.G. van Pol, J. Quebert, P. Roussel-Chomaz, Y. Schutz, A. Schubert, R.H. Siemssen, R.S. Simon, Z. Sujkowski, V. Wagner, and H.W. Wilschut, Phys. Lett. B **334**, 23 (1994).

[21] S. Riess, G. Enders, A. Hofmann, W. Kuhn, V. Metag, R. Novotny, W. Mittig, Y. Schutz, A.C.C. Villari, H. Emling, H. Grein, E. Grosse, W. Henning, R. Holzmann, R. Kulessa, T. Matulewicz, and H.J. Wollersheim, Phys. Rev. Lett. **69**, 1504 (1992).

[22] T. Reposeur, J. Clayton, W. Benenson, M. Cronquist, S. Hannuschke, S. Howden, J. Karn, D. Krofcheck, A. Nadasen, C. Ogilvie, R. Pfaff, J.D. Stevenson, A. Vander Molen, G.D. Westfall, K. Wilson, J.S. Winfield, and B. Young, Phys. Lett. B **276**, 418 (1992).

[23] E. Migneco, C. Agodi, R. Alba, G. Bellia, R. Coniglione, A. Del Zoppo, P. Finocchiaro, C. Maiolino, P. Piattelli, G. Raia, and P. Sapienza, Nucl. Instrum. Methods Phys. Res. A **314**, 31 (1992).

[24] A. Del Zoppo, C. Agodi, R. Alba, G. Bellia, R. Coniglione, P. Finocchiaro, C. Maiolino, E. Migneco, A. Peghaire, P. Piattelli, and P. Sapienza, Nucl. Instrum. Methods Phys. Res. A **327**, 363 (1993).

[25] D.G. Sarantites, L.G. Sobotka, T.M. Semkov, V. Abenante, J. Elson, J.T. Hood, Z. Li, N.G. Nicolis, D.W. Stracener, and J. Valdes, Nucl. Instrum. Methods Phys. Res. A **264**, 319 (1988).

[26] T. Suomijarvi, Y. Blumenfeld, P. Piattelli, J.H. Le Faou, C. Agodi, N. Alamanos, R. Alba, F. Auger, G. Bellia, Ph. Chomaz, R. Coniglione, A. Del Zoppo, P. Finocchiaro, N. Frascaria, J.J. Gaardhoje, J.P. Garron, A. Gillibert, M. Lamehi-Rachti, R. Liguori-Neto, C. Maiolino, E. Migneco, G. Russo, J.C. Roynette, D. Santonocito, P. Sapienza, J.A. Scarpaci, and A. Smerzi, Phys. Rev. C **53**, 2258 (1996).

[27] A. Chbihi, L.G. Sobotka, Z. Majka, D.G. Sarantites, D.W. Stracener, V. Abenante, T.M. Semkow, N.G. Nicolis, D.C. Hensley, J.R. Beene, and M.L. Halbert, Phys. Rev. C **43**, 652 (1991).

[28] K. Yoshida, J. Kasagi, H. Hama, M. Sakurai, M. Kodama, K. Furutaka, K. Ieki, W. Galster, T. Kubo, M. Ishihara, and A. Galonsky, Phys. Rev. C **46**, 961 (1992).

[29] A. Fahli, J.P. Coffin, G. Guillaume, B. Heusch, F. Jundt, F. Rami, P. Wagner, P. Fintz, A.J. Cole, S. Kox, and Y. Schutz, Phys. Rev. C **34**, 161 (1986).

[30] D. Jouan, B. Borderie, M.F. Rivet, C. Cabot, H. Fuchs, H. Gauvin, C. Gregoire, F. Hanappe, D. Gardes, M. Montoya, B. Remaud, and F. Sebille, Z. Phys. A **340**, 63 (1991).

[31] P.R. Bevington, *Data Reduction and Error Analysis for the Physical Sciences* (McGraw-Hill, New York, 1969), p. 237.

[32] T.C. Awes, G. Poggi, C.K. Gelbke, B.B. Back, B.G. Glagola, H. Breuer, and V.E. Viola, Jr., Phys. Rev. C **24**, 89 (1981).

[33] T.C. Awes, S. Saini, G. Poggi, C.K. Gelbke, D. Cha, R. Legrain, and G.D. Westfall, Phys. Rev. C **25**, 2361 (1982).

[34] C.J. Gelderloos, Rulin Sun, N.N. Ajitanand, J.M. Alexander, E. Bauge, A. Elmaani, T. Ethvignot, R.A. Lacey, M.E. Brandan, A. Giorni, D. Heuer, S. Kox, A. Lleres, A. Menchaca-Rocha, F. Merchez, D. Rebreyend, J.B. Viano, B. Chambon, B. Cheynis, D. Drain, and C. Pastor, Phys. Rev. C **52**, 3488 (1995).

[35] L. Beaulieu, R. Laforest, J. Pouliot, R. Roy, C. St-Pierre, G.C. Ball, E. Hagberg, D. Horn, and R.B. Walker, Nucl. Phys. **A580**, 81 (1994).

[36] D. Sackett, A. Galonsky, C.K. Gelbke, H. Hama, L. Heilbronn, D. Krofcheck, W. Lynch, H.R. Schelin, M.B. Tsang, X. Yang, F. Deák, Á. Horváth, Á. Kiss, Z. Seres, J. Kasagi, and T. Murakami, Phys. Rev. C **44**, 384 (1991).

[37] M.F. Rivet, B. Borderie, P. Box, M. Dakowski, C. Cabot, D. Gardes, D. Jouan, G. Mamane, X. Tarrago, H. Utsonomiya, Y. El Masri, F. Hanappe, F. Sebille, and F. Haddad, in Proceedings of the XXXI International Winter Meeting on Nuclear Physics, Milano, 1993, edited by I. Iori, p. 92.

[38] E. Crema, S. Bresson, H. Doubre, J. Galin, B. Gatty, D. Guerrau, D. Jacquet, U. Jahnke, B. Lott, M. Morjean, E. Piaseki, J. Pouthas, F. Saint-Laurent, E. Schwinn, A. Sokolov, and X.M. Wang, Phys. Lett. B **258**, 266 (1991).

[39] M. Gonin, L. Cooke, B. Fornal, P. Gonthier, M. Gui, Y. Lou, J.B. Natowitz, G. Nardelli, G. Nebbia, G. Prete, R.P. Schmitt, B. Srivastava, W. Turmel, D. Utley, H. Utsonomiya, G. Viesti, R. Wada, B. Wilkins, and R. Zanon, Nucl. Phys. **A495**, 139c (1989).

[40] R. Alba, R. Coniglione, A. Del Zoppo, C. Agodi, G. Bellia, P. Finocchiaro, K. Loukachine, C. Maiolino, E. Migneco, P. Piattelli, D. Santonocito, P. Sapienza, A. Peghaire, I. Iori, L. Manduci, and A. Moroni, Phys. Lett. B **322**, 38 (1994).

[41] B.V. Jacak, G.D. Westfall, G.M. Crawley, D. Fox, C.K. Gelbke, L.H. Harwood, B.E. Hasselquist, W.G. Lynch, D.K. Scott, H. Stocker, M.B. Tsang, and G. Buchwald, T.J.M. Symons, Phys. Rev. C **35**, 1751 (1987), and references therein.

[42] J. Peter, J.P. Sullivan, D. Cussol, G. Bizard, R. Brou, M. Louvel, J.P. Patry, R. Regimbart, J.C. Steckmeyer, B. Tamain, E. Crema, H. Doubre, K. Hagel, G.M. Jin, A. Peghaire, F. Saint-Laurent, Y. Cassagnou, R. Legrain, C. Lebrun, E. Rosato, R. Macgrath, S.C Jeong, S.M. Lee, Y. Nagashima, T. Nakagawa, M. Ogihara, J. Kasagi and T. Motobayashi, Phys. Lett. B **237**, 187 (1990).

[43] W.E. Ormand, P.F. Bortignon, A. Bracco, and R.A. Broglia, Phys. Rev. C **40**, 1510 (1989).

[44] J.B. Natowitz, R. Wada, K. Hagel, T. Keutgen, M. Murray, A. Makeev, L. Qin, P. Smith, and C. Hamilton, Phys. Rev. C **65**, 034618 (2002).

[45] J.J. Gaardhoje, Annu. Rev. Nucl. Part. Sci. **42**, 483 (1992).

[46] G. Bellia, R. Alba, R. Coniglione, A. Del Zoppo, P. Finocchiaro, C. Maiolino, E. Migneco, P. Piattelli, P. Sapienza, N. Frascaria, I. Lhenry, J.C. Roynette, T. Suomijärvi, N. Alamanos, F. Auger, A. Gillibert, D. Pierroutsakou, J.L. Sida, and P.R. Silveira Gomes, Nucl. Instrum. Phys. Res. A **329**, 173 (1993).

[47] G. Bellia, Nuovo Cimento A **71**, 370 (1982).

[48] G. Bellia, A. Del Zoppo, E. Migneco, and G. Russo, Nucl. Instrum. Methods Phys. Res. A **226**, 424 (1984).

[49] A.R. Lampis, J. Stevenson, W. Benenson, J. Clayton, D. Cebra, Y. Chen, D. Fox, E. Kashy, D.J. Morrissey, M. Samuel, R. Smith, C.L. Tam, G.D. Westfall, K. Wilson, and J.S. Winfield, Phys. Rev. C **38**, 1961 (1988).

[50] A. Del Zoppo, P. Sapienza, R. Alba, R. Coniglione, E. Migneco, C. Agodi, G. Bellia, P. Finocchiaro, K. Loukachine, C. Maiolino, A. Peghaire, P. Piattelli, and D. Santonocito, Nucl. Phys. **A583**, 363 (1995).

[51] P. Piattelli, D. Santonocito, Y. Blumenfeld, T. Suomijarvi, C. Agodi, N. Alamanos, R. Alba, F. Auger, G. Bellia, Ph. Chomaz, M. Colonna, R. Coniglione, A. Del Zoppo, P. Finocchiaro, N. Frascaria, A. Gillibert, J.H. Le Faou, K. Loukachine, C. Maiolino, E. Migneco, J.C. Roynette, P. Sapienza, and J.A. Scarpaci, Phys. Lett. B **442**, 48 (1998).

[52] B. Remaud, C. Grégoire, F. Sébille, and P. Schuck, Nucl. Phys. **A488**, 423c (1988); F. Haddad, F. Sébille, M. Farine, V. de la Mota, P. Schuck, and B. Jouault, Phys. Rev. C **52**, 2013 (1995).

[53] G.F. Bertsch and S. Das Gupta, Phys. Rep. **160**, 190 (1988).

[54] M. Colonna, N. Colonna, A. Bonasera, and M. Di Toro, Nucl. Phys. **A541**, 295 (1992).

[55] A. Guarnera, Ph.D. thesis, University of Caen, 1996.

[56] A. Bonasera, F. Gulminelli, and J. Molitoris, Phys. Rep. **243**, 1 (1994).